Curved atmospheric rivers and their moisture remnants: a new detection tool for Antarctica

Victoire Buffet[1,2], Vincent Favier[1], Benjamin Pohl[2], Jonathan D. Wille[1]

[1]Université Grenoble Alpes/CNRS/IRD/G-INP, IGE, Grenoble, 38000, France
[2]Biogéosciences, UMR6282 CNRS / Université Bourgogne Europe, Dijon, 21000, France

Correspondence to: Victoire Buffet (victoire.buffet@univ-grenoble-alpes.fr)

Abstract. Atmospheric rivers (ARs) represent the main intrusions of moisture and heat into Antarctica, exerting a major influence on the continent's surface mass balance. Yet, due to geometric and directional constraints, existing detection algorithms often fail to track their evolution inland after landfall or in regions where abrupt directional changes occur. We introduce DARK (Detecting ARs using their Kurvature), a new Antarctic AR detection framework designed to overcome these limitations. DARK applies a strict 98th-percentile threshold to total integrated vapor transport and computes AR length along the curved axis to evaluate the 2000-km AR criterion. This enables the continuous detection of ARs with complex geometries, including those that curve, overturn, or extend across the South Pole. An additional AR-children module identifies smaller but still intense moisture remnants that detach from parent ARs after landfall yet continue to transport vapor and heat inland. The resulting climatology shows that DARK ARs account for about 18 % of total Antarctic precipitation and are linked to roughly half of top 1 % daily precipitation anomalies, 60 % of top 1 % daily maximum temperature anomalies, and 80 % of compound warm-and-wet events. DARK provides a more detailed assessment of AR-related precipitation and temperature impacts in the South Pole region. Despite slightly higher occurrence, risk ratio analysis shows that DARK ARs more effectively capture the most intense events than earlier Antarctic schemes. Including AR-children further strengthens these associations, especially over Victoria Land, where they contribute to about one third of AR-related precipitation.

Plain Language Summary. Atmospheric rivers (ARs) are long, narrow bands of air that carry large amounts of moisture and heat from the lower latitudes into Antarctica, where they trigger snowfall, surface melt, and extreme temperature events. Existing tools to detect these features often miss them when they arrive at the coast in unusual directions or continue moving inland after landfall. We developed a new detection method, called DARK, that can identify atmospheric rivers regardless of their shape or direction, including those that curve or cross the South Pole. DARK also tracks smaller moisture remnants, called AR-children, that split off from the main system after it reaches the continent but continue to bring moisture inland. Our results show that atmospheric rivers detected by DARK are responsible for about 18 % of Antarctic snowfall and are associated with half of the top 1 % precipitation anomaly days, 60 % of the top 1 % warm anomaly days, and 80 % of days with simultaneous top 1 % warm and precipitation anomalies. AR-children make additional contributions, particularly in Victoria Land. This new framework provides a more complete picture of how atmospheric rivers shape the weather and mass balance of the Antarctic Ice Sheet.

Keywords : Atmospheric rivers – Antarctica – Precipitation – Detection tool – Methodology

1 Introduction

Atmospheric rivers (ARs) are long, narrow filaments of enhanced horizontal water vapor transport that are an essential component of the global hydrological cycle and particularly play a central role in the Antarctic surface mass balance (e.g. Zhu and Newell, 1998; Wille et al., 2025). ARs contribute positively to the Antarctic Ice Sheet (AIS) mass balance through enhanced snowfall (Turner et al., 2019; Wille et al., 2021; Maclennan et al., 2022), but they can also induce surface melt and promote ice-shelf instability when transporting warm, moist air masses inland (Gorodetskaya et al., 2014; Adusumilli et al., 2021; Wille et al., 2019; Wille et al., 2022). Given their dual role, robust detection of ARs is essential for quantifying their frequency and impacts.

Many AR detection tools (ARDTs) have been developed for different purposes and regions (Collow et al., 2022), but only a few are tailored to polar environments (Wille et al., 2021; Gorodetskaya et al., 2014; Mattingly et al., 2018; Wille et al., 2025). At the global scale, the most widely used scheme remains that of Guan and Waliser (2015), recently updated in Guan and Waliser (2024). It employs seasonally and spatially varying vertically integrated water vapor transport (IVT) thresholds (85th percentile), which provide broad applicability and robust intercomparison across reanalyses (Collow et al., 2022). The method also applies a set of geometric and directional filters, including a minimum feature length of about 2000 km, a length-to-width ratio requirement to ensure narrow filamentary structures, and directional coherence criteria that retain only elongated, dynamically consistent moisture transport features. In its latest version (Guan and Waliser, 2024; hereafter G&W v4), several refinements were introduced, including a revised treatment of directional coherence, improved handling of zonally oriented ARs in the extratropics, and a polar refinement based on a hemispheric IVT threshold, defined from the area-weighted spatial

5th percentile of local IVT thresholds. This replaces the previously fixed 100 kg $m^{-1}s^{-1}$ minimum and allows ARs to extend farther inland in polar regions. Despite these advances, limitations remain over Antarctica. Because the threshold is based on hemispheric IVT climatology, its effective local percentile varies strongly across the continent. It corresponds to relatively low local percentiles in West Antarctica and coastal regions, favoring numerous AR detections, but to very high percentiles over the cold, dry East Antarctic interior, sometimes exceeding the 99th percentile, which prevents inland detections. Consequently, AR occurrence remains spatially heterogeneous, with frequent detections along the coast and in West Antarctica but few over much of the East Antarctic Ice Sheet.

For Antarctica, the most widely used polar-specific ARDT is that of Wille et al. (2021), which includes two variants of the same method applied to different input variables: the meridional component of IVT (vIVT, hereafter Wille vIVT) and vertically integrated water vapor (IWV, hereafter Wille IWV). Among these, the vIVT-based version is the most commonly used. It applies a monthly, locally defined 98th-percentile threshold on vIVT, combined with a 20° meridional extent criterion, to identify the strongest southward moisture intrusions linking the lower latitudes to the Antarctic continent. This design is physically consistent with the dynamics of extreme Antarctic precipitation, as intense snowfall events are generally associated with above-average IVT directed southward and approximately perpendicular to the coast (Wille et al., 2021). Consequently, the Wille vIVT scheme effectively isolates the ARs that have been linked to intense precipitation (Wille et al., 2021; Maclennan et al., 2022), surface melt (Wille et al., 2019, Gorodetskaya et al., 2023), firn depletion, large iceberg calving events, and ice-shelf destabilization (Wille et al., 2022). Thus, this ARDT has become the reference framework for polar AR studies (Wille et al., 2025).

However, the Wille et al. (2021) framework, while robust, does not capture the full range of intense moisture transport features relevant to Antarctica. While weaker or more diffuse intrusions are rightly excluded by design, some long, narrow, and intense filaments of water vapor transport, dynamically consistent with the physical definition of ARs (American Meteorological Society, 2022), remain undetected. This underdetection arises from methodological constraints related to the orientation, coherence, and geometric requirements of the detection scheme.

First, the use of vIVT in the Wille vIVT scheme introduces a discontinuity at the South Pole. When an AR crosses the pole, the sign of vIVT reverses from poleward to equatorward, preventing its identification. This discontinuity also breaks the continuity of the feature's axis, preventing it from satisfying the minimum length criterion (20° meridional extent) at the highest latitudes. This issue does not affect the Wille IWV scheme, which does not consider the meridional wind; however, Wille et al. (2021) restricted their detection domain to 85° S (Fig. 1b) to avoid this singularity, in both vIVT and IWV schemes, to maintain consistency of AR climatologies between both algorithms. While this boundary had little impact on coastal AR landfalls and when tracking their progression inland, it introduces a progressive detection bias toward lower latitudes, up to around 65° S, as a result of the 20° meridional-extent requirement.

Second, focusing on “moisture transport axes”, a term introduced to unify ARs, tropical moisture exports, and warm moist intrusions; Spensberger et al. (2025) note that one third of those axes exhibit an equatorward component. This behavior likely reflects synoptic-scale processes such as frontal occlusion and the curvature of moisture pathways within mature cyclones, as well as the modulation of moisture transport by quasi-stationary large-scale circulation features and topographic forcing. As these systems move poleward and their associated ARs approach the Antarctic coast, they interact with the prevailing near-surface easterlies and the steep topography of the ice sheet margin. These interactions often cause the moisture plumes to curve or tilt at landfall, deviating from a purely meridional orientation. Approximately 20% of “moisture transport axes” south of 70° S display such equatorward curvature (Spensberger et al., 2025). This behavior is particularly common in the Ross Sea and Weddell Sea regions (see Fig. 1a for geographic regions referenced in this study), where synoptic and orographic effects jointly steer moisture fluxes away from the meridional direction. In these cases, vIVT decreases and reverses sign as the AR curves equatorward, leading to a loss of detection at and beyond the inflection point. Although this specific limitation does not affect the Wille IWV scheme, it remains constrained by the 20° meridional-extent criterion, which also excludes long, curved, or overturning ARs that are dynamically consistent with AR characteristics but have limited meridional span due to their complex geometry. This limitation is not unique to the Wille vIVT and IWV frameworks. Global AR detection schemes such as G&W v4 also apply directional-coherence constraints that may limit the detection of ARs with strongly curved or reversing geometries, though their primary limitation over Antarctica relates to the effective IVT threshold rather than directionality, as further discussed in Sect. 3.

Another limitation of existing detection approaches concerns the evolution of ARs after they reach the Antarctic continent. As they make landfall, they often diverge and lose their narrow filamentary geometry due to condensation, latent heat release, and the spreading of moisture fluxes within occluding or decaying frontal systems (Dacre and Clark, 2025). Although this morphological transition causes them to fall outside the geometric criteria of standard AR detection methods, these features frequently remain highly moisture-laden and continue to drive precipitation, cloud formation, and surface melt inland. To capture the continuation of AR influence, identifying and tracking such post-landfall remnants would be relevant but has not yet been proposed. This would allow the monitoring of structures representing the inland evolution of decaying but still active AR-provided moisture remnants. Accounting for these structures would be essential for quantifying the sustained hydrological and thermodynamic effects of ARs on the Antarctic surface mass balance, while extending the study of the Antarctic AR life cycle to its terminus (Wille et al., 2024).

To address these limitations, we develop a new Antarctic ARDT called DARK (Detecting ARs using their Kurvature), that builds upon the intensity-based framework of Wille et al. (2021) while removing directional constraints that limit the identification of curved or equatorward-turning ARs (like the AR making landfall on 2020-11-16, in Dronning Maud Land, Fig. 1b). The method applies a 98th-percentile threshold on total integrated vapor transport (IVT), computed using a 15-day rolling window to capture temporal variability and regional seasonality. Features smaller than 200,000 km² are removed prior

to classification. ARs are then defined as contiguous structures exceeding the IVT threshold with a total length of at least 2000 km, approximately equivalent to the 20° meridional extent criterion of Wille et al. (2021) (Fig. 1b), but regardless of their orientation or directional coherence. In addition, we introduce an add-on to identify and track post-landfall moisture remnants with IVT above the local 98th-percentile, with an area exceeding 20,000 km², which evolve from previously detected ARs but no longer meet the geometric length criterion, hereafter referred to as AR-children. This study aims to illustrate that our framework provides a more complete and physically consistent view of AR-driven moisture transport and its influence on Antarctic precipitation and near-surface temperature variability, with implications for surface melt and ice-shelf stability.

We apply this framework to a multi-decadal ERA5 reanalysis (1979–2023) to produce the first comprehensive assessment of Antarctic ARs detected by DARK (hereafter DARK ARs) and their post-landfall AR-children. The analysis quantifies their contribution to Antarctic precipitation, as well as to precipitation, temperature, and compound extreme anomalies. It further characterizes the magnitude and orientation of IVT and presents representative case studies illustrating their synoptic evolution. Throughout, DARK is compared against the Wille vIVT, Wille IWV, and G&W v4 catalogues to contextualize its added value. This framework aims to fill key observational and methodological gaps left by existing ARDTs, providing a more comprehensive representation of Antarctic ARs and their impacts on the AIS.

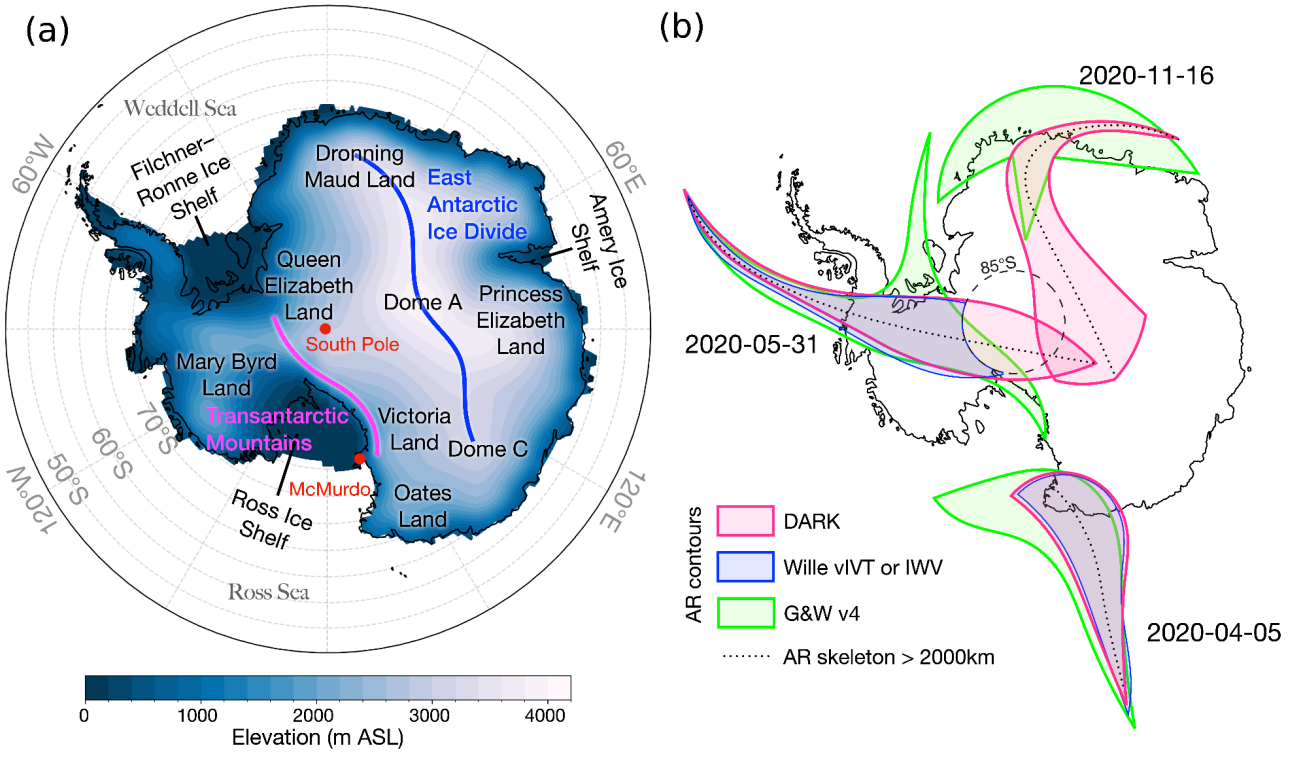

Figure 1. (a) Map of the Antarctic Ice Sheet showing surface elevation (m a.s.l.) and key geographic regions discussed in the text. (b) Conceptual schematic illustrating detection differences between the DARK, Wille AR and G&W v4 frameworks during three arbitrary yet representative landfall events.

2 Data and methodology

2.1 Data

We use the ERA5 reanalysis produced by the European Centre for Medium-Range Weather Forecasts (ECMWF; Hersbach et al., 2020) for the period 1979–2023, at a horizontal resolution of 0.25° × 0.25°. Atmospheric rivers are detected at 6-hourly intervals using the eastward (uIVT) and northward (vIVT) components of integrated vapor transport (IVT). Diagnostic variables, including wind and geopotential height at 500 hPa, are analyzed at the same 6-hourly timestep. Surface diagnostics are evaluated at daily resolution: total precipitation is aggregated to daily sums, and 2 m air temperature is used to derive daily maximum values.

For intercomparison, the Wille et al. (2021) Antarctic AR detection schemes based on integrated water vapor (IWV) and meridional IVT (vIVT) were recomputed at 6-hourly intervals. To ensure spatial consistency with the new DARK framework, both Wille schemes were extended northward to 15° S while retaining their original southern boundary at 85° S. This adjustment provides uniform temporal and spatial coverage across methods, enabling a direct comparison of AR frequency, geometry, and associated surface impacts over the 1979–2023 period.

We additionally use the tARget version 4 AR catalog (Guan and Waliser, 2024; hereafter referred to as G&W v4), generated from ERA5 for 1940–2023. Only the 1979–2023 period is retained to match the analysis window used throughout this study.

2.2 DARK AR Detection Algorithm

At each 6-hourly time step, the DARK framework is applied over the 15° S-90° S domain. The magnitude of IVT is computed from its zonal and meridional components as

$$IVT = \sqrt{uIVT^2 + vIVT^2} \quad (1)$$

where $uIVT$ and $vIVT$ are the zonal and meridional components of IVT from ERA5.

A rolling 15-day 98th-percentile threshold of IVT is calculated for each grid point and day of year using all available years (1979–2023). Grid cells exceeding this threshold are identified at each 6-hourly time step and grouped into contiguous features using a connectivity criterion that links all directly adjacent or diagonally touching cells (Fig. 2a). Objects smaller than 200,000 km² are removed (consistent with the typical spatial scale of ARs, which are generally hundreds of kilometres wide and at least

2,000 km long) before centerline computation to avoid processing small, isolated exceedances that are not representative of large-scale moisture transport and for which centerline estimation is computationally expensive and prone to numerical error (Fig. 2b).The remaining features are processed to extract a smoothed centerline (Fig. 2d,e). An object is classified as an AR if the geodesic length of this centerline equals or exceeds 2000 km, consistent with the typical length scale used in established AR detection frameworks (Fig. 2f; e.g., Guan and Waliser, 2015; Guan and Waliser, 2024; Wille et al., 2021; Skinner et al., 2020; Gorodetskaya et al., 2014). This procedure yields a binary AR mask indicating the presence or absence of an AR at each grid point and time step.

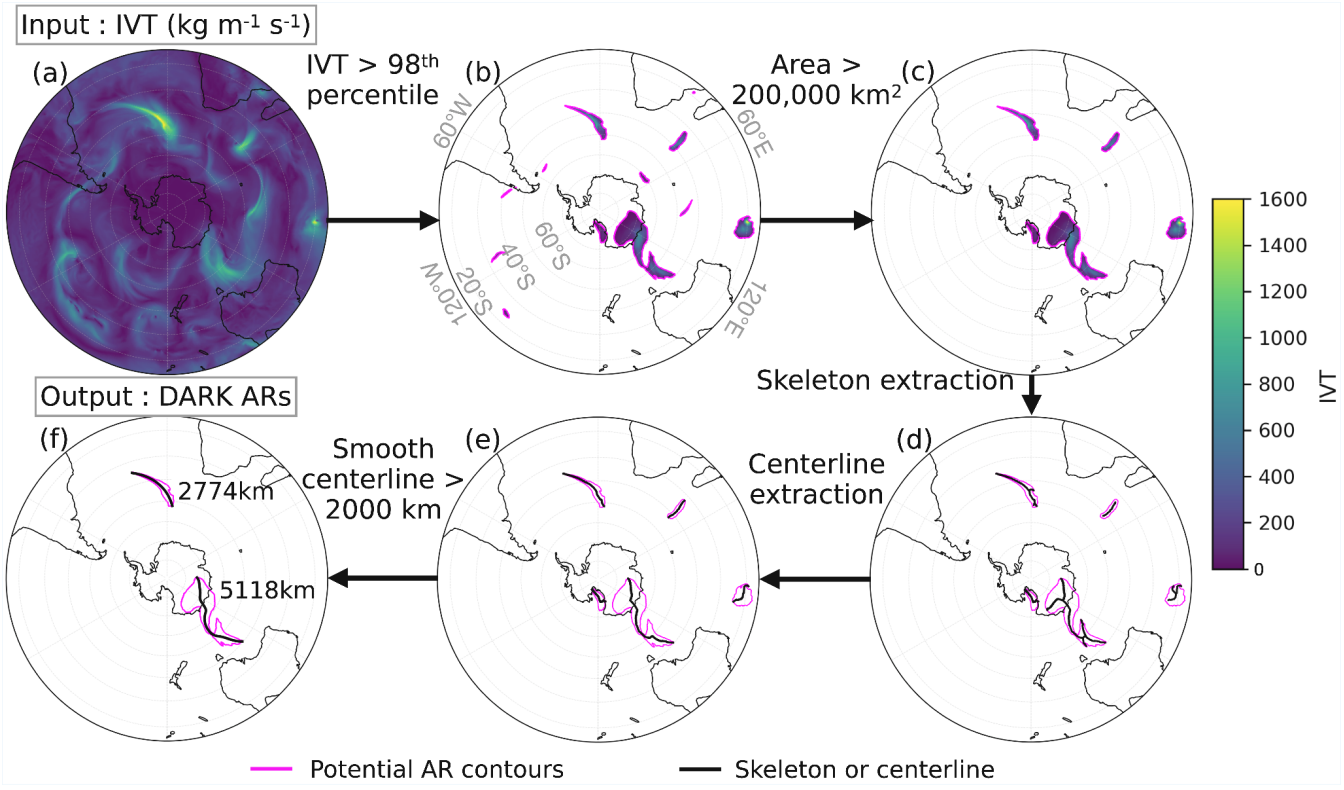

Figure 2. Schematic overview of the DARK detection workflow applied to a single 6-hourly ERA5 time step. (a) Total IVT field used as input. (b) Grid cells exceeding the local 98th-percentile threshold. (c) Objects with an area exceeding 200,000 km² retained. (d) Skeleton extracted from each remaining object. (e) Smoothed centerline derived from the skeleton. (f) Final DARK AR classification: objects whose centerline geodesic length equals or exceeds 2000 km are retained, with their centerline length indicated in km. Magenta contours show the potential (b–e) or final (f) AR object boundaries and black lines show the skeleton (d), centerline (e) or smoothed centerline (f).

2.3 Optional AR-children add-on

The AR-children add-on is an optional extension of the main detection algorithm. It builds upon the AR catalog described above to identify post-landfall moisture structures that remain intense after the parent AR loses spatial coherence. Accordingly, two catalogs are provided: one including only DARK ARs and another combining DARK ARs with their AR-children, with accompanying binary and classification variables (see Data Availability). At each time step, regions where IVT exceeds the 98th-percentile threshold are labeled as contiguous features using a connectivity criterion that links all directly adjacent or diagonally touching grid cells. Temporal continuity is established through spatial overlap between consecutive time steps, ensuring consistent tracking of moisture structures while maintaining computational efficiency. A feature is classified as an AR-child when it previously overlaps with a detected parent AR and subsequently detaches from it while being in contact with, or located over, the Antarctic continent. A minimum area of 20,000 km² is imposed to exclude small structures. This approach ensures both physical and temporal consistency while remaining computationally efficient for multi-decadal, hemispheric reanalysis datasets.

The AR-children module requires approximately 9h of CPU time and ~17 GB of memory for the full 1979–2023 climatology, compared to 1h and ~8 GB for the core DARK algorithm (see Code and Data Availability section).

2.4 Attribution of events to ARs

To attribute surface impacts to ARs (or AR-children), we identify precipitation and temperature events associated with AR occurrence at each grid cell. Because AR-related precipitation and temperature anomalies can persist beyond the period when a given grid cell is directly affected by an AR, the attribution window is extended to include adjacent days, depending on the variable.

For precipitation, AR-related events are defined as those occurring on the day of AR landfall (D_0) and the following day (D_{+1}), following Wille et al. (2021) and Maclennan et al. (2022). We use here a daily timescale for computing efficiency and to avoid multiple detections of single extreme events due to serial correlation at sub-daily timescales. This extension accounts for residual precipitation that continues after the main AR plume loses coherence or moves inland.

For temperature, AR-related events are considered on the day before (D_{-1}), the day of (D_0), and the day after (D_{+1}) AR landfall. This accounts for both preconditioning (e.g., warm advection ahead of the AR) and lagged warming due to persistent cloud cover, latent heat release, or surface melt following AR passage.

For precipitation, daily totals are compared to the mean daily climatology for each calendar day (1979–2023), while for 2 m air temperature, daily maxima are compared with the corresponding daily-maximum climatology. In both cases, the anomaly represents the deviation from the daily mean climatological value at each grid point.

Extreme events are defined as days when these anomalies exceed the 99th percentile of their respective daily anomaly distributions, computed independently at each grid point. Compound events, defined as the co-occurrence of extreme precipitation and temperature anomalies, are identified when an extreme precipitation day coincides with or occurs within ±1 day of an extreme temperature anomaly. This temporal window ensures that temporally overlapping or closely spaced extremes are captured within a single compound-event framework. This approach allows both direct and short-lagged compound extremes associated with ARs to be included in the analysis.

2.5 Characterisation of AR moisture transport directionality

To characterise the directionality of moisture transport during AR events, we analyse the ERA5 IVT components ($uIVT$ and $vIVT$; eastward and northward respectively) at each grid cell and 6-hourly time step flagged as an AR over the 1979–2023 period. Three metrics are computed for each grid cell. First, the fraction of AR time steps where meridional flow dominates (i.e. $|vIVT| > |uIVT|$) is computed as a percentage of all AR time steps at that grid cell; the complementary fraction corresponds to zonal-dominant flow $|uIVT| > |vIVT|$). Second and third, the fraction of AR time steps with eastward ($uIVT > 0$) and northward ($vIVT > 0$) IVT are computed likewise.

2.6 Risk Ratio

Because extending the attribution window naturally increases the number of AR-associated events, we quantify their statistical relevance using risk ratios (RR; Katz et al., 1978; Scholz and Lora, 2024). This ensures that higher counts reflect genuine physical associations rather than the effect of broader temporal inclusion. RR are computed as the ratio between the probability of an extreme event during AR conditions (Eq. 2) and the probability during non-AR conditions (Eq. 3).

For each grid point, the conditional probabilities are defined as:

$$P(E \mid AR) = \frac{N_{E,AR}}{N_{AR}} \quad (2)$$

$$P(E \mid \neg AR) = \frac{N_{E,\neg AR}}{N_{\neg AR}} \quad (3)$$

where $N_{E,AR}$ is the number of days with both an AR and an extreme event (considering the temporal extension defined in Sect. 2.6), N_{AR} is the total number of AR days (including the temporal extensions defined in Sect. 2.6), $N_{E,\neg AR}$ is the number of extreme events without an AR, and $N_{\neg AR}$ the number of non-AR days. RR is then expressed as:

$$RR = \frac{P(E|AR)}{P(E|\neg AR)} \quad (4)$$

Values of $RR > 1$ indicate that extreme events are more likely under AR conditions. For example, a value of $RR = 2$ implies that extreme events are twice as likely to occur during AR conditions compared to non-AR conditions. This metric accounts for the frequency of AR occurrence, ensuring that results reflect the relative enhancement of extremes rather than the prevalence of ARs themselves.

2.7 Statistical significance

Differences in AR occurrence between schemes were evaluated using a two sample test of equality of proportions at each grid point. For the share of precipitation attributable to ARs, as well as for extreme precipitation, temperature, and compound events, significance was assessed using the same bootstrap framework: AR dates (including their variable-dependent temporal extensions) were kept fixed, while entire precipitation or temperature years were permuted without replacement, preserving their autocorrelation and seasonality but breaking their co-occurrence with ARs. The observed AR-associated fraction (or the difference between detection schemes) was compared against 1000 bootstrap realizations, and values were considered significant when they lay outside the corresponding 95 % bootstrap confidence interval.

The statistical significance of the RRs was assessed following the log-normal approximation method of Katz et al. (1978), because the distribution of the risk ratio is asymmetric while its logarithm is approximately normally distributed, allowing reliable confidence intervals to be derived using standard normal theory. To handle zero count cases, we applied the Haldane–Anscombe correction (Haldane, 1940; Anscombe, 1956) by adding 0.5 to both co-occurrence counts and 1 to the total-event denominators. A 95 % confidence interval was computed on the log-transformed RR and then exponentiated back to the RR scale. Grid cells were considered significant when the confidence interval excluded 1; otherwise, they were masked as non-significant.

3 Results

3.1 Frequency of DARK ARs and AR-children

DARK ARs exhibit their highest occurrence within the midlatitude storm-track regions (~50°S, Fig. 3a; Chemke et al., 2022) (Chang et al., 2002; Wirth et al., 2018), with maxima during austral winter (see Fig. S1). The lowest frequencies occur over the Ross Sea sector, where the minimum is most pronounced in winter. The spatial distribution closely matches that of Wille vIVT and Wille IWV schemes, although DARK ARs yields higher overall frequencies, particularly over the AIS. Over South of the East Antarctic Ice Divide (EAID, Fig. 1a), occurrence is up to 1.2 percentage points (pp) higher than in Wille vIVT and IWV, while along the East Antarctic coast the difference remains small (≈ 0.3 pp), indicating that the total frequency of AR

landfalls along the Antarctic coastline remains roughly unchanged between the Wille and DARK schemes. By construction, AR-children occur exclusively over the continent and its coastal margins, with mean frequencies up to 0.3 % along the coast and local maxima of 0.6 % near McMurdo and farther inland over the plateau (Fig. S2a), bringing the total frequency of DARK ARs and their AR-children at 1.5 % across most of the AIS (Fig. 3b).

The G&W v4 scheme exhibits a strikingly different spatial distribution of AR occurrence from both DARK and the Wille schemes. On average, G&W v4 detects 4.4 pp more AR occurrence than DARK across the Antarctic continent, but this average conceals an extreme spatial heterogeneity. Along the coast of West Antarctica, the Antarctic Peninsula, and the broader AIS coastline, G&W v4 exceeds DARK by up to 10 pp, while inland, south of the East Antarctic Ice Divide, DARK detects up to 1.3 pp more than G&W v4 (Fig. 3a). This sharp gradient is further illustrated in Fig. S2: G&W v4 detects more than 2000 AR days at the coastline but fewer than 10 South of the EAID over the full 1979–2023 period, compared to around 400 for DARK and around 300 for the Wille schemes. This sharp coastal-to-inland gradient reflects a fundamental limitation of the G&W v4 hemispheric threshold for capturing the full lifecycle of Antarctic ARs, and results in detection frequencies that are either far in excess of or far below those of DARK and the Wille schemes across most of the continent, with only a narrow transitional zone where they are broadly comparable. While G&W v4 effectively detects the most intense moisture intrusions at the coast, where IVT is highest, its effective threshold of 46.8 kg $m^{-1}s^{-1}$ in January and 39.4 kg $m^{-1}s^{-1}$ in July (Guan and Waliser, 2024) prevents detection of ARs as they penetrate inland and progressively lose intensity. As shown in Fig. S2, mean AR IVT values for DARK and the Wille schemes decrease to 10 kg m^{-1} s^{-1} or below south of the EAID, well below the G&W v4 effective threshold, and G&W v4 records no detections (Fig. S2) at all over some interior regions such as Dome A and the area surrounding the South Pole. This suggests that G&W v4 captures the arrival of the most intense ARs at the Antarctic margin, but is not designed to monitor their inland penetration and associated surface impacts on the ice sheet.

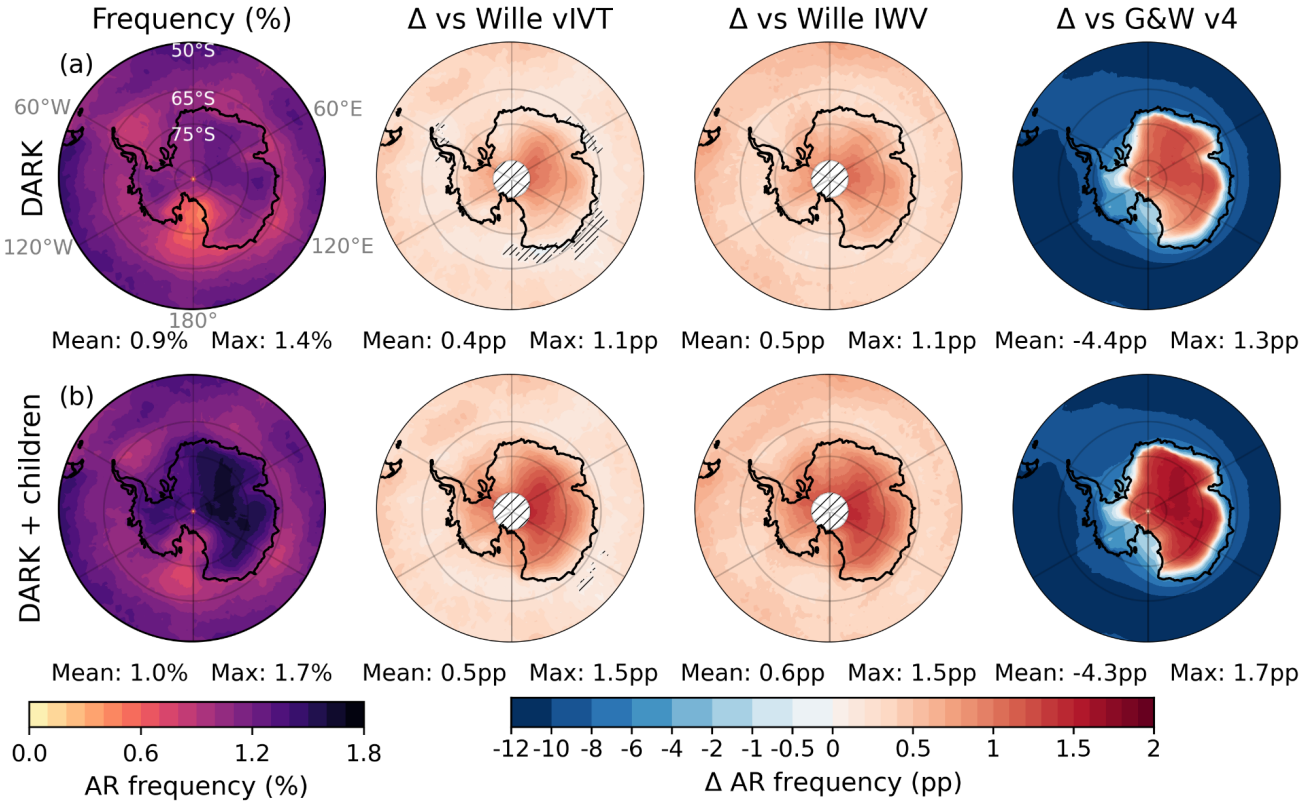

Figure 3. Frequency of DARK atmospheric rivers (ARs) (a) and DARK ARs and their children (b) from 60° S to 90° S. From left to right: AR occurrence (%), differences from the Wille vIVT, the Wille IWV and the G&W v4 schemes (percentage points, pp). Hatched white areas south of 85° S mark regions without data in the Wille schemes, hatches elsewhere cover non-significant regions (Sect. 2.7). Land-area weighted mean and maximum values are indicated below each panel.

3.2 Direction and orientation of DARK ARs

DARK ARs exhibit a much wider range of orientations than either Wille schemes while still reproducing well the dominant large-scale IVT orientation patterns (zonal versus meridional, and eastward versus westward) captured by Wille IWV (Fig. 4a, c; Sect. 2.5). A majority of Wille vIVT ARs are also detected by DARK, with 64 % agreement over the Southern Ocean and about 61 % on average across the AIS (Fig. S5a). The co-detection is strongest where DARK ARs exhibit predominantly meridional, southward orientations, such as over southern Dronning Maud Land, Coats Land, and along the northern flank of the East Antarctic Ice Divide. However, a substantial fraction of ARs detected by DARK are not captured by Wille vIVT: across the Antarctic Ice Sheet, roughly 67 % of DARK ARs are exclusive to the new detection framework (Fig. S5b). These additional detections are particularly frequent from the Ross Ice Shelf to Dome A along the southern flank of the East Antarctic

Ice Divide. In these regions, DARK ARs are mainly northward (Fig. 4c; and eastward, due to the influence of the East Antarctic topography and the Coriolis deflection of the pressure-driven circulation) oriented, which is incompatible with Wille's strict requirement of southward vIVT. Elsewhere across the continent, all three schemes, DARK, Wille vIVT, and Wille IWV, show predominantly southward-oriented ARs, confirming that most intense moisture transport toward Antarctica occurs in a poleward direction. Wille vIVT ARs that do occur there generally correspond to relatively strong meridional, but weak total IVT, since the percentile-based threshold can be met even under low IVT. In contrast, DARK detects ARs in these sectors because they exceed the 98th-percentile threshold in total IVT, capturing dynamically stronger but more geometrically complex structures. Compared with Wille IWV, DARK shows a more homogeneous agreement across the AIS, with up to 90 % co-detection in Dronning Maud Land (Fig. S5a). This higher overlap reflects the greater directional flexibility of Wille IWV, which can capture zonal or northward ARs (Fig. 4a,c), including those turning over the Ross and Amery Ice Shelves and along the East Antarctic coastline. However, Wille IWV remains limited by its 20° meridional-extent criterion, which disfavors fully zonal filaments. Moreover, because IWV represents static moisture rather than dynamic transport, it detects only about 50 % of DARK ARs in localized regions such as the Dronning Maud Land coast (Fig. S5b). These undetected cases typically contain high humidity but insufficient wind to produce large IVT values, preventing them from meeting the DARK threshold. Overall, Wille vIVT and IWV ARs only partially overlap with DARK detections. A majority of Wille (vIVT or IWV) ARs are identified by DARK, but many DARK ARs are not detected by Wille ARDTs. This asymmetry highlights that while the methods share a common physical basis, DARK extends beyond Wille's directional and geometric constraints, capturing a more dynamically coherent and diverse range of AR geometries, including curved, zonal, and poleward-turning filaments that were missed by previous frameworks.

Compared with G&W v4, DARK shows broadly consistent large-scale IVT orientation patterns across both the Southern Ocean and the Antarctic continent, although the G&W v4 fields appear noisier over the interior due to the very low number of detections in these regions.

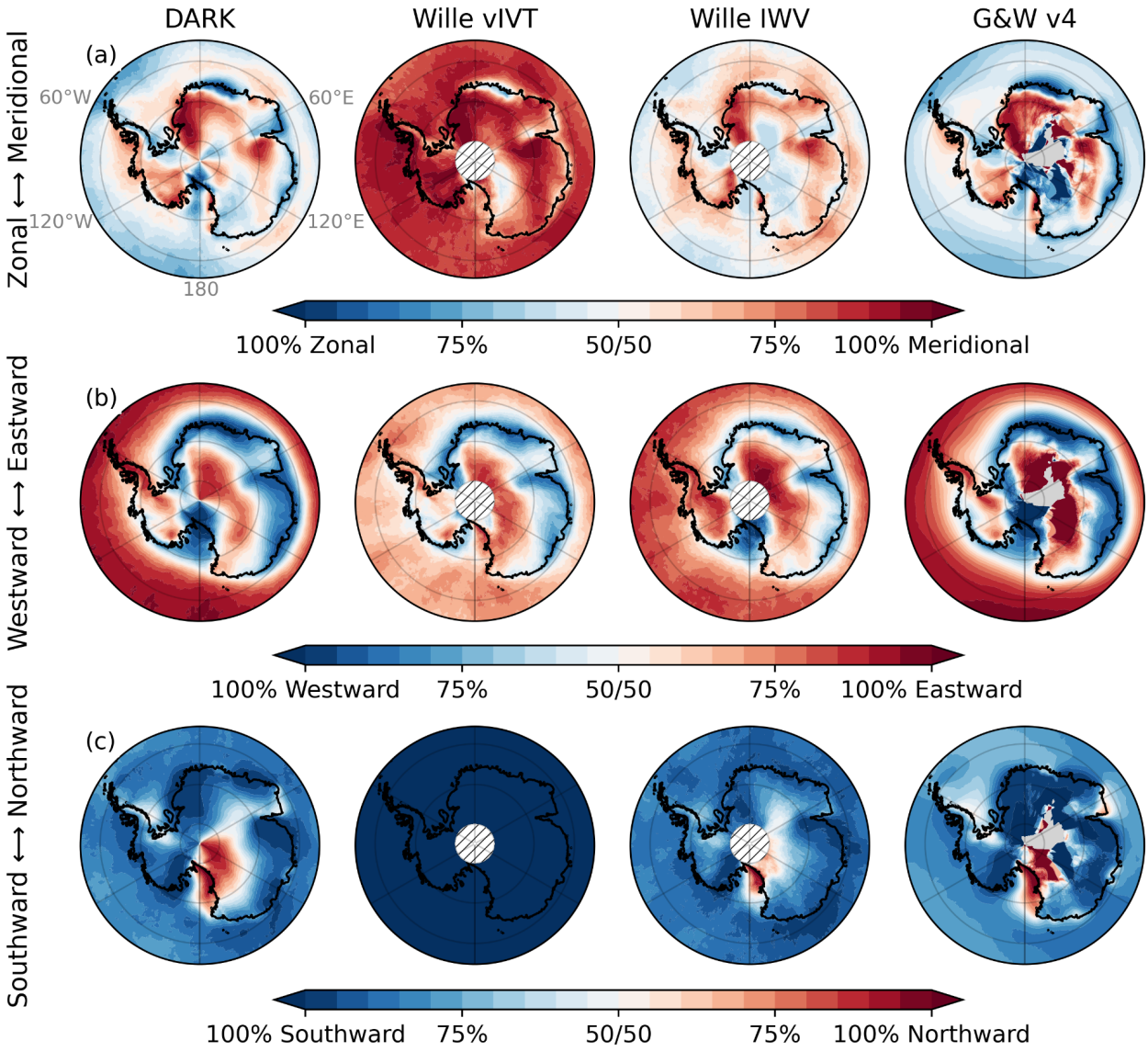

Figure 4. Fraction of AR time characterized by (a) zonal vs. meridional dominant IVT components (|uIVT| vs. |vIVT|), (b) westward vs. eastward uIVT, and (c) southward vs. northward vIVT, for each AR catalogue (from left to right: DARK, Wille vIVT, Wille IWV and G&W v4). Hatched white areas south of 85° S mark regions without data in the Wille schemes. Grey shading in the G&W v4 column indicates grid cells where no AR was detected over the full period.

3.2 Contribution of ARs to Antarctic precipitation

DARK ARs account for an average of 18 % of total AIS precipitation, reaching up to 35 % in some regions (Fig. 5a). Only along the relatively straight, zonally oriented sectors of the East Antarctic coastline, their contribution is comparable to that of Wille vIVT ARs. In contrast, in areas where the coastline geometry departs from this alignment, particularly within the major embayments such as the Ross, Ronne–Filchner, and Amery Ice Shelves, DARK ARs contribute to substantially more precipitation, with enhanced signals extending inland over the catchments located south of the EAID. The only region where DARK ARs contribute to less precipitation than Wille vIVT ARs is Oates Land.

On average, DARK ARs deliver 5 (8) pp more precipitation than Wille vIVT (Wille IWV), with local increases up to 18 (20) pp in the interior, notably near the South Pole and the Transantarctic Mountains. Even when both Wille schemes are combined, DARK ARs still produce 2 pp more precipitation on average, with local differences reaching up to 15 pp (Fig. S6). The comparison with G&W v4 reveals spatially contrasting differences that cannot be summarized by the AIS-averaged difference alone, as the two schemes have fundamentally different detection footprints over Antarctica. Along the coast and over the WAIS, the very high AR occurrence in G&W v4 translates into substantially more attributed precipitation, locally exceeding DARK by up to 50 pp. Moving inland, this signal reverses sharply: DARK explains up to 24 pp more precipitation north of the EAID, where G&W v4 detections drop off rapidly due to its effective hemispheric IVT threshold. This coastal dominance outweighs the inland gains, yielding a slightly negative AIS-averaged difference of -3 pp (Fig. 5a, right column). This sign reversal reflects the different purposes of the two approaches: G&W v4 was designed for global applicability and captures intense coastal moisture intrusions, while DARK was specifically designed to monitor AR activity across the full Antarctic continent, including its interior. Within the DARK framework itself, AR-children contribute little on average (Fig. 5b) but represent a significant additional source within these embayments, most notably over the Amery Ice Shelf and Victoria Land, where they account for more than 8 % of total AIS precipitation (Fig. S2b).

In this analysis, precipitation occurring on the day of AR landfall (D_0) and the following day (D_{+1}) is attributed to ARs throughout this study (Sect. 2.4), and to ARs and their children when using the DARK+children framework, consistent with common practice (Wille et al., 2021; Maclennan et al., 2022). When AR-children are included, however, a comparable AIS-averaged share of precipitation is obtained (Fig. S7) even when considering precipitation associated with DARK ARs and their children on the day of landfall alone (D_0), compared to attributing precipitation to DARK ARs without including AR-children over both the day of landfall (D_0) and the following day (D_{+1}). This reflects not a temporal substitution, but a spatial refinement: AR-children explicitly capture the inland propagation and dissipation of moisture that, in previous approaches, was only approximated by extending the temporal attribution window beyond landfall. Their inclusion therefore provides a more physically consistent representation of post-landfall hydrological impacts.

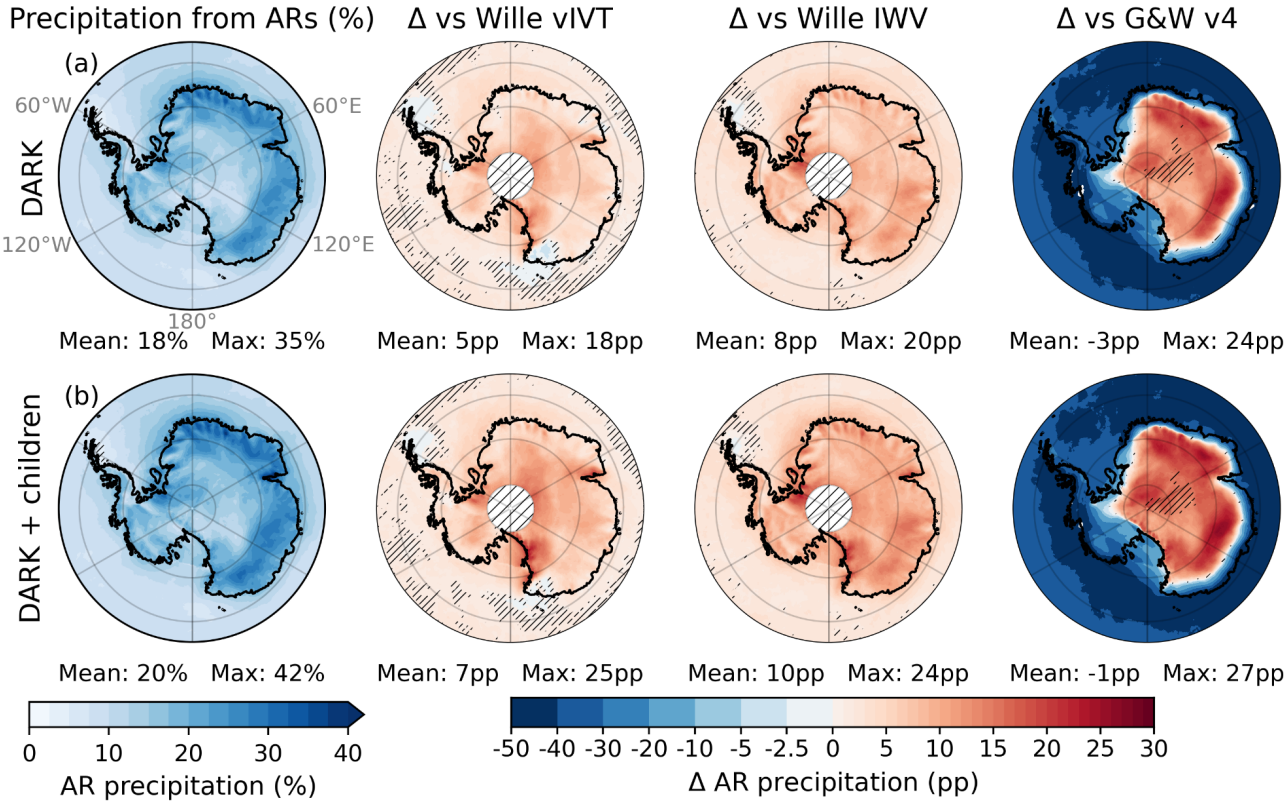

Figure 5. Share of total precipitation attributed (Sect. 2.4) to (a) DARK ARs and (b) DARK ARs and their children. From left to right: percentage of precipitation from ARs, differences from the Wille vIVT, the Wille IWV, and the G&W v4 schemes (pp). Antarctic land-only (inside-coastline) mean and maximum values are reported below each panel. Hatched white areas south of 85° S mark regions without data in the Wille schemes, hatches elsewhere cover non-significant regions (Sect. 2.7).

While DARK ARs contribute more to precipitation than either Wille scheme across most of the AIS, this increase primarily reflects their higher occurrence frequency rather than higher precipitation per event (Fig. 6a). When normalized by AR occurrence, that is, expressed as the ratio of AR-related precipitation (%) to AR occurrence (%), the mean precipitation intensity (pp pp^{-1}, dimensionless) associated with DARK ARs is slightly lower overall than in both Wille schemes (around -5). Relative to Wille IWV, precipitation intensity is lower across the AIS in a broadly uniform pattern. However, relative to Wille vIVT, differences are more heterogeneous: intensity is reduced over most of the AIS but locally enhanced over the Amery Ice Shelf and south of the EAID, peaking along the Ross sector of the Transantarctic Mountains (up to 34). When DARK ARs and their associated children are considered together, the overall AR intensity further decreases, although they remain more intense than Wille ARs in the latter regions (Fig. 6b).

The comparison with G&W v4 mirrors the spatial heterogeneity seen in total precipitation. Along the coast and over the WAIS, DARK ARs are more intense than G&W v4 ARs (positive differences), consistent with DARK having fewer but still highly impactful detections in these regions. Inland, the picture reverses: intensity differences become negative over large parts of the East Antarctic interior, reaching below −50 in some areas. These strongly negative values, however, must be interpreted with caution, as they correspond to regions where G&W v4 detects very few AR days over the full period (fewer than 35 where differences exceed −50, fewer than 100 where they exceed −30; Fig. S4). In these areas, the small sample of G&W v4 detections consists almost exclusively of the most intense inland moisture intrusions, inflating their mean intensity relative to DARK. Overall, this confirms that G&W v4 selectively captures the most intense moisture intrusions at the coast and in the rare inland locations where IVT remains sufficiently high, while missing the broader population of intrusions that DARK and the Wille schemes track from the coast into the interior.

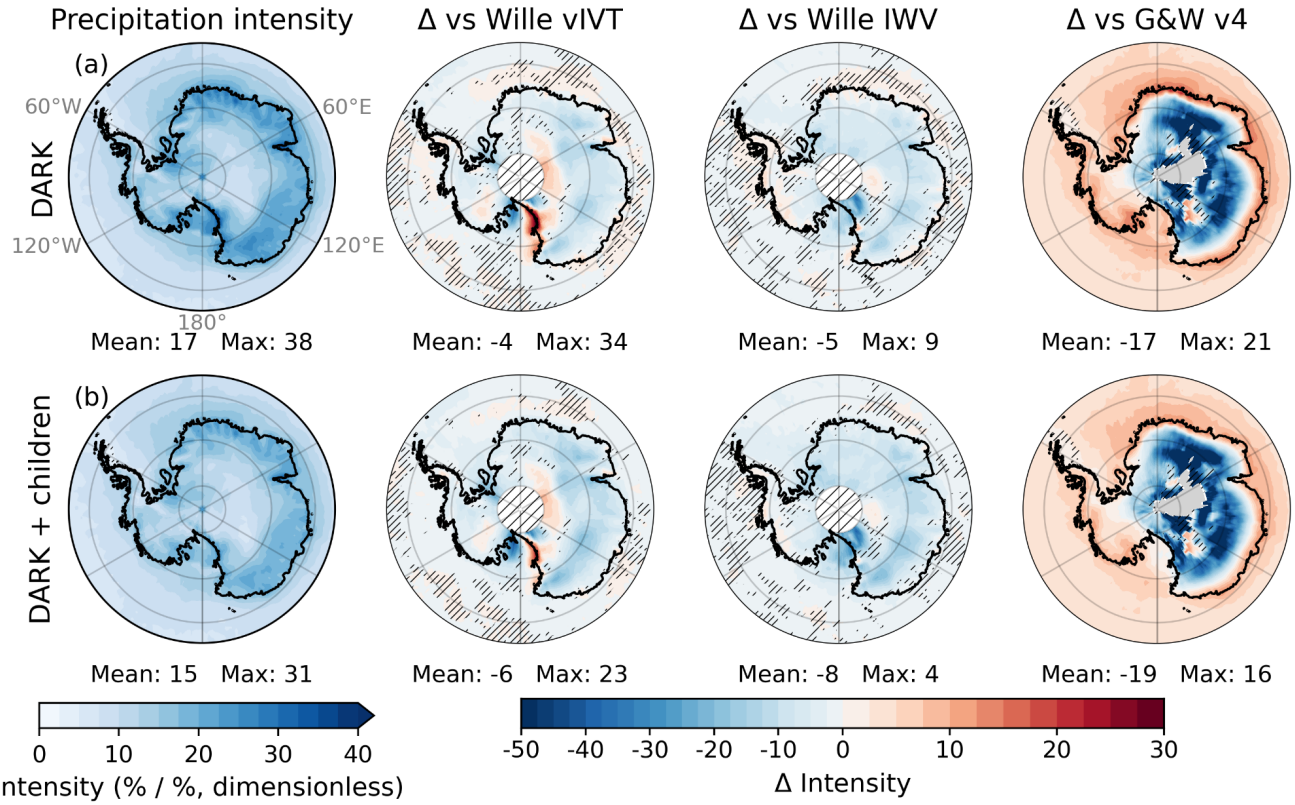

Figure 6. Normalized AR precipitation intensity, defined as the ratio between the percentage of precipitation from ARs (Fig. 3) and AR frequency (Fig. 3, unitless), for (a) DARK ARs and (b) DARK ARs and their children. From left to right: differences from the Wille vIVT, the Wille IWV, and the G&W v4 schemes (pp). Antarctic land-only mean and maximum values are

reported below each panel. Hatched white areas south of 85° S mark regions without data in the Wille schemes, hatches elsewhere cover non-significant regions (Sect. 2.7)

3.3 Contribution to extreme events

DARK ARs are associated with 53 % of extreme (Sect. 2.4) precipitation days on average (Fig. 7a), with local values reaching up to 85 % inland of the East Antarctic coast and decreasing toward Dome C. Although the mean precipitation per AR event is lower (Sect. 3.2), the DARK scheme captures a substantially larger proportion of the most intense precipitation anomalies than either Wille scheme. Compared to Wille vIVT, the association fraction is higher by 15 pp on average and locally by up to 56 pp south of the EAID, with only a few small areas showing slightly weaker associations, the largest being Oates Land. Relative to Wille IWV, the increase is more spatially homogeneous, with the largest differences following topography, particularly over Queen Elizabeth Land. This pattern indicates that DARK, like Wille vIVT, better represents topographically induced precipitation linked to moisture transport rather than static humidity. Compared with G&W v4, DARK explains on average 10 pp more extreme precipitation days across the AIS, with gains up to 81 pp inland. Along the coast and over the WAIS, G&W v4 associates more extreme days with ARs, consistent with its very high detection frequency in these regions. However, unlike for total precipitation, the AIS-averaged difference remains positive, reflecting the fact that many of the numerous G&W v4 coastal detections are associated with non-extreme precipitation events that do not reach the top 1% threshold. Including AR-children increases the mean association by only about 5 pp (Fig. 7a,b), but they remain locally significant, forming broad hotspots over the Amery Ice Shelf and across Victoria Land, where they account for more than 15 %, and locally up to 20 %, of extreme precipitation days (Fig. S8). These regions represent the strongest and most spatially extensive contributions of AR-children, while more localized contributions also occur south of the EAID, where post-landfall moisture remnants sustain intense precipitation after the parent AR dissipates.

DARK ARs are associated with 67 % of extreme daily maximum temperature events on average (Sect. 2.4; Fig. 7c), with local values exceeding 80 % near Dome C and over Dronning Maud Land. Compared to the Wille schemes, DARK increases the association fraction by more than 28 pp on average. The gain is spatially uniform relative to Wille IWV and more spatially contrasted compared to Wille vIVT, with the largest improvements south of the EAID. Compared with G&W v4, DARK explains on average 22 pp more extreme temperature days, with a spatially uniform inland advantage reflecting DARK's more consistent continental coverage. As with precipitation extremes, G&W v4 explains more along the coast, but the AIS-averaged difference remains strongly positive, consistent with DARK's broader and more homogeneous detection across the interior. Including AR-children further raises the mean association to approximately 71 % (Fig. 7d), primarily through a uniform increase of about 4 pp across most of the AIS. In several regions, this leads to association fractions exceeding 90 % locally, while the largest increases occur over Victoria Land and the Ross Ice Shelf–McMurdo area, where AR-children contribute up to 20 pp of additional extreme temperature events. This reflects the persistence of warm, moist air masses following AR landfall (Fig. S8).

Compound (precipitation and 2 m air temperature) extremes (Sect. 2.4) occur widely across Antarctica but are absent leeward of the Antarctic Peninsula, where strong foehn winds produce warm but dry conditions (Fig. S9). DARK ARs are associated with approximately 78 % of compound extremes on average (Fig. 8a) and with nearly 100 % across broad sectors of East Antarctica. DARK identifies substantially more inland events than Wille vIVT, which captures many compound events along the coast but misses large interior regions south of the EAID, from southern Dronning Maud Land to Victoria Land and around the Amery Ice Shelf. Compared with G&W v4, DARK explains on average 30 pp more compound extremes across the AIS, with the same coastal-to-inland polarity as for precipitation and temperature extremes. Including AR-children increases the mean association modestly (by about 3 pp) but introduces a distinct new hotspot over Victoria Land (Fig. 8b), where AR-children contribute to more than 20 pp of additional compound extremes (Fig. S8). Notably, Victoria Land is also one of the two main regions of frequent compound events across the continent, although such events remain rare overall (fewer than 0.5 % of days: Fig. S9).

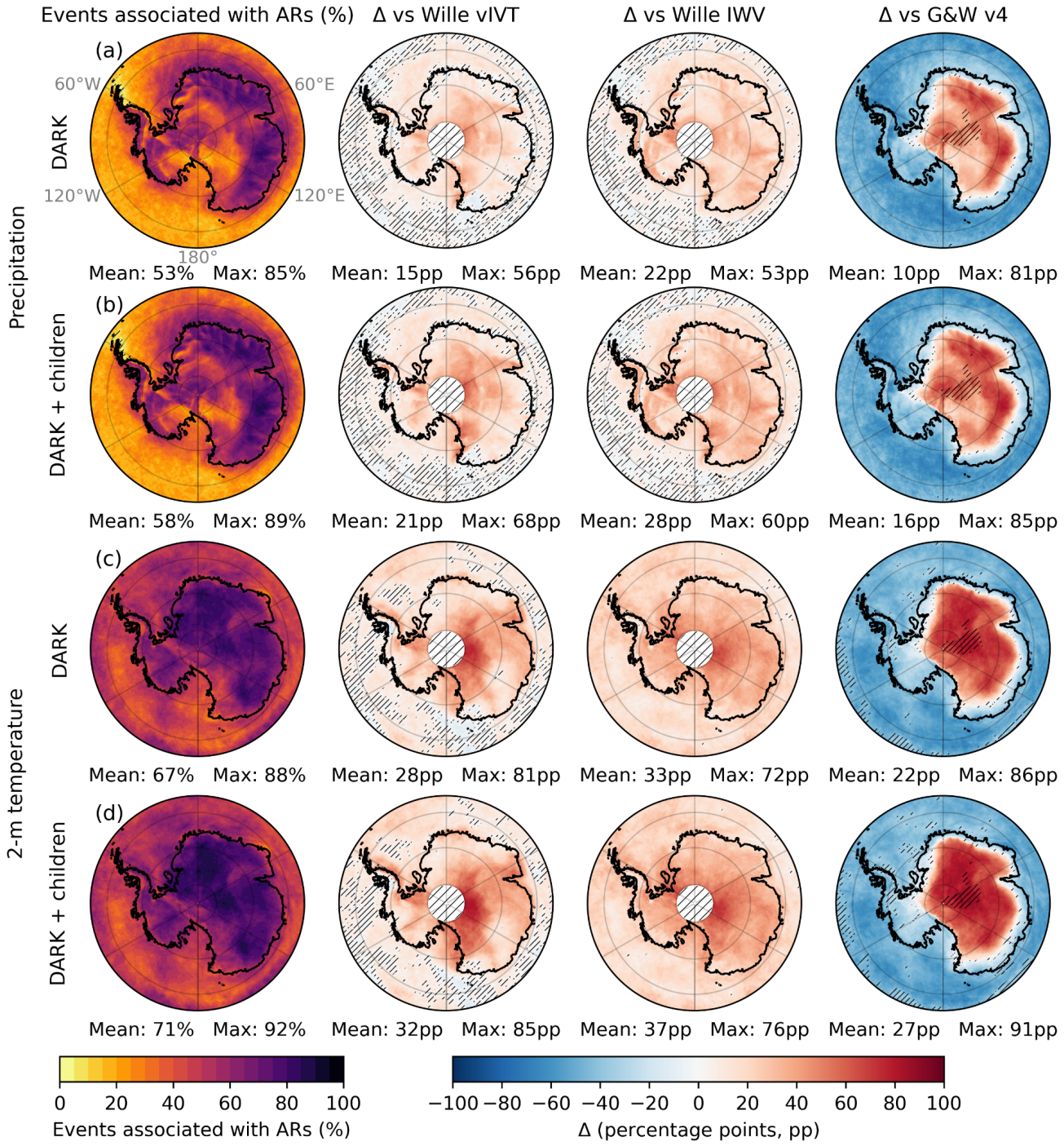

Figure 7. Fraction of 99th-percentile anomaly days associated with DARK ARs for precipitation (rows a–b) and 2 m temperature (rows c–d). Within each variable, the first row shows DARK ARs and the second row shows DARK ARs + children. Columns show (left to right) the absolute fraction of extremes and the differences relative to the Wille vIVT,the Wille

IWV, and the G&W v4 schemes (percentage points, pp). Antarctic land-only mean and maximum values are reported below each panel. Hatched white areas south of 85° S mark regions without data in the Wille schemes; hatched overlays indicate non-significant values (Sect. 2.7); grey shading indicates grid cells with no detected extremes.

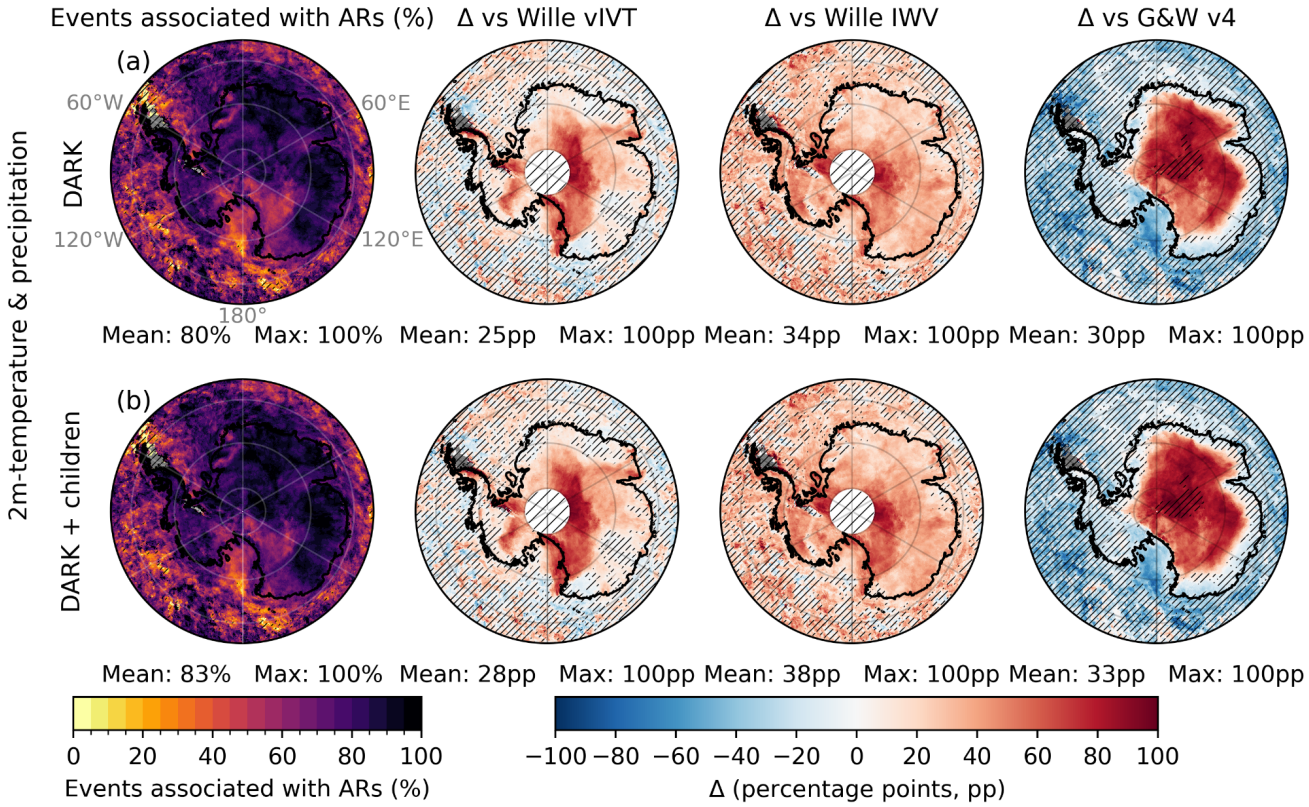

Figure 8. Fraction of compound extreme days combining 99th-percentile precipitation and 2 m air temperature anomalies associated with DARK ARs. Row (a) shows DARK ARs and row (b) shows DARK ARs and their children. From left to right: the absolute fraction of compound extremes and the differences relative to the Wille vIVT,the Wille IWV, and the G&W v4 schemes (percentage points, pp). Antarctic land-only mean and maximum values are reported below each panel. Hatched white areas south of 85° S mark regions without data in the Wille schemes; hatched overlays indicate non-significant values (Sect. 2.7); grey shading indicates grid cells with no detected compound extremes.

Risk ratios (RR) are next used to account for differences in AR occurrence frequency (Sect. 2.6). For precipitation, DARK yields RR values comparable to or higher than those of the Wille schemes across most of the AIS (Fig. 9a), indicating that extreme precipitation is about 30 times more likely during an AR, independently from the selected ARDT. The spatial pattern closely resembles that of Wille vIVT, with the highest values north of the EAID and local peaks reaching 142. However, for 2 m air temperature (Fig. 9b), the similarity with Wille's ARDTs is weaker. While DARK reproduces the main hotspots seen

in Wille's ARDTs, RRs are considerably larger over a much wider area. The Antarctic-wide mean RR reaches 45 (roughly twice the Wille means), with local maxima up to 143, demonstrating that DARK not only amplifies the temperature hotspots detected by Wille vIVT and IWV but also identifies additional regions of strong AR influence beyond those captured by the original scheme. For compound extremes (Fig. 9c), DARK produces a markedly higher RR than Wille's ARDTs, with an Antarctic-wide mean of 128, almost double that of Wille's 's ARDTs, and local maxima exceeding 10^3, highlighting the dominant influence of ARs on concurrent warm and wet extremes. Including AR-children further increases both mean and peak RR for precipitation, temperature, and compound events, illustrating that post-landfall moisture remnants can cause extremes after the parent AR loses coherence.

The G&W v4 ARDT yields substantially larger RR values across the AIS for all variables (Fig. 9). For precipitation (Fig. 9a), the Antarctic-wide mean RR reaches 71, more than twice the values obtained with DARK and the Wille schemes. A similar difference is found for 2 m air temperature (Fig. 9b), where the mean RR rises to 76. For compound extremes (Fig. 9c), the Antarctic-wide mean RR reaches 146. These large ratios reflect a very strong statistical association between G&W v4 ARs and extreme events. However, their magnitude is strongly shaped by the particular spatial structure of G&W v4 detection frequency over Antarctica, with far more AR days than DARK or the Wille schemes at the coast and far fewer inland, which creates strongly contrasted AR and non-AR pools that mechanically amplify RR in both regimes. The spatial coincidence between the largest RR values and the regions of highest G&W v4 detection frequency is a direct consequence of these contrasts, rather than evidence of a stronger physical association. Consequently, the RR values from G&W v4 are less directly comparable to those obtained with DARK and Wille's ARDTs.

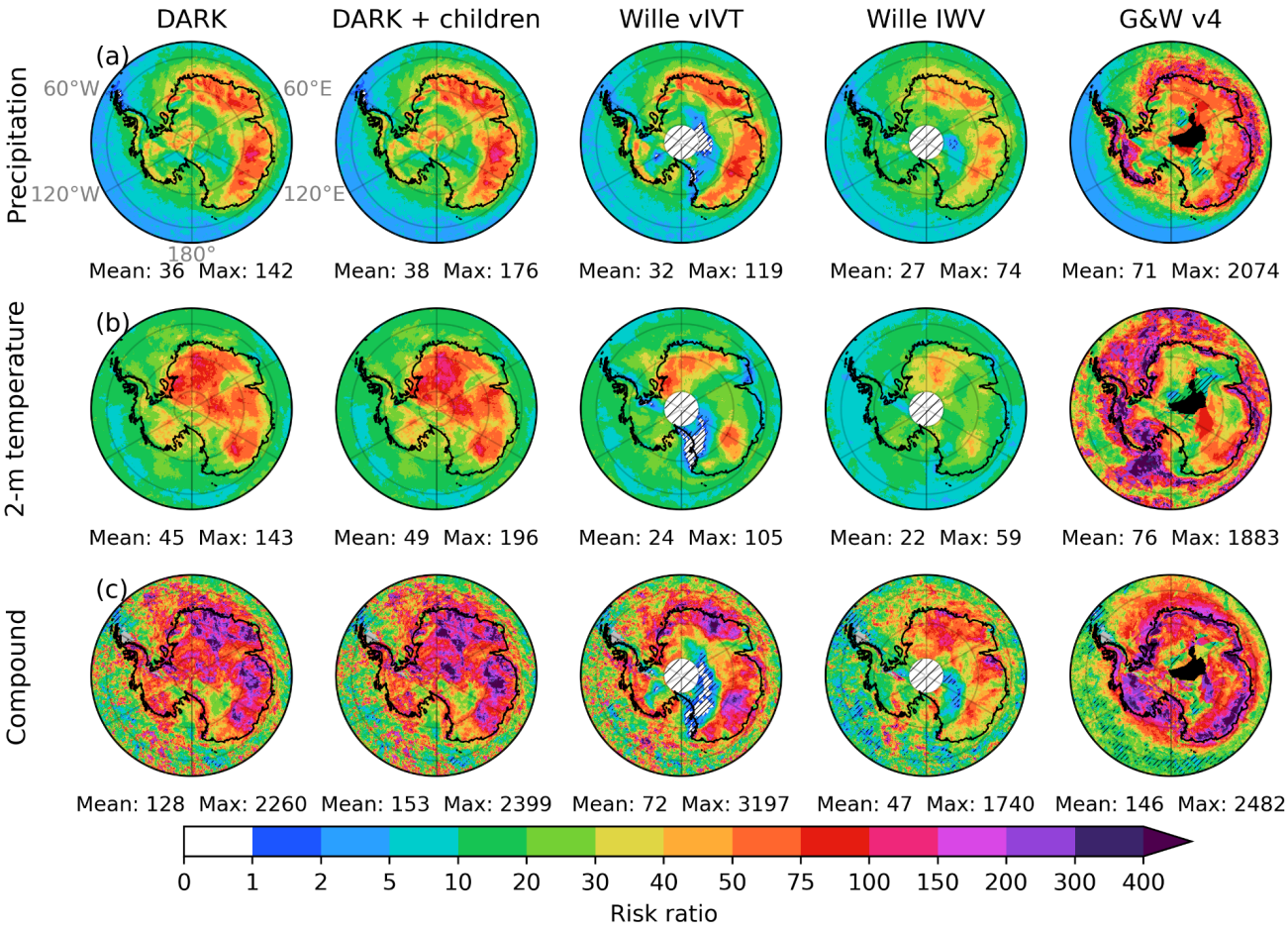

Figure 9. Risk ratio (RR; see Sect. 2.6) of 99th-percentile anomalies during AR conditions for (a) 2 m air temperature, (b) precipitation, and (c) compound events (precipitation + temperature; see Sect. 2.4). Columns correspond to DARK ARs, DARK ARs and their children, Wille vIVT, Wille IWV, and G&W v4 ARs. Values of RR > 1 indicate an increased likelihood of extremes under AR conditions. Grey areas indicate grid cells without detected compound extremes, hatches indicate non-significant RR (Sect. 2.7), black shading in the G&W v4 column indicates grid cells where no AR was detected over the full period.

3.4 Regional case studies

To illustrate the performance of the DARK framework during intense to extreme weather events, we analyze representative cases. The first case study focuses on the McMurdo region, a well-known area situated between the Ross Ice Shelf and Victoria

Land, both of which show strong enhancement in DARK relative to Wille's ARDTs. The second case study examines ARs detected south of the EAID, including those crossing the South Pole.

3.4.1 Extreme events in the McMurdo–Dry Valleys region

The first case study focuses on the McMurdo–Dry Valleys domain (160–168° E, 78.5–77.5° S), where two exceptional events exemplify the synoptic conditions driving major precipitation and temperature extremes.

On 1 December 2003 (Fig. 10a), the McMurdo-Dry Valleys region recorded more than 16 mm of precipitation, exceptionally high for this arid environment, representing the largest daily precipitation total in the 1979–2024 ERA5 dataset. Including the following day (2 December 2003, with more than 12 mm, corresponding to the 99.9th percentile), the two day total accounts for over 14 % of the annual precipitation in 2003. The 500-hPa geopotential height anomalies reveal a broad anticyclonic circulation spanning the Antarctic interior from the Bellingshausen Sea to Dome C, with a maximum over Marie Byrd Land. The western flank of this ridge directed a zonal moisture flux into the western Ross Sea sector. Upon encountering the Transantarctic Mountains, this flux curved equatorward and westward, producing intense coastal precipitation. The DARK scheme captures the full curvature of this moisture filament as it arcs inland over Victoria Land, while neither Wille vIVT nor Wille IWV detect the equatorward-turning portion (Fig. 10a). G&W v4 detects a broader moisture feature over the Ross Sea and Victoria Land, capturing part of the zonal flux but not the full inland portion of what DARK classifies as an AR. Notably, G&W v4 flags numerous AR objects across the Southern Hemisphere on this date, considerably more than DARK or the Wille schemes, reflecting its lower effective IVT threshold in high-IVT coastal regions. The precipitation maximum coincides with the AR's interaction with the Transantarctic Mountains, followed by a sharp inland decline in IVT consistent with strong orographic precipitation. By 2 December, a deep trough northwest of the Ross Sea had aligned and channeled moisture from the South Pacific toward the Ross Ice Shelf, sustaining the precipitation event. The main AR filament had dissipated, leaving behind a remnant classified as an AR-child, while G&W v4 captures this day as a full AR extending from the South Pacific, detecting the entire moisture import corridor where DARK identifies only the inland tip. Despite its smaller spatial extent, this remnant produced more than 12 mm of precipitation, still within the top 0.1 % of daily values. This demonstrates that post-landfall AR fragments can sustain extreme precipitation even after the parent AR loses coherence. This event highlights the importance of explicitly identifying and tracking AR-children, which can prolong the hydrological impacts of ARs well beyond their formal duration.

On 9 July 2019 (Fig. 10b), an exceptional temperature extreme affected the Ross Ice Shelf region, including the McMurdo area, with 2 m air temperature daily anomalies peaking at +27.9 °C in the McMurdo-Dry Valleys. This event represents the largest daily-mean temperature anomaly in the 1979–2024 ERA5 record, and exceeded +31 °C over parts of the shelf. The 500-hPa geopotential height anomalies show an extensive anticyclonic structure extending from the southern tip of South America across the Antarctic continent and into the southern Indian Ocean, centered over the Antarctic interior. A deep trough

north of the Ross Sea directed moist air from the South Pacific toward the Ross Ice Shelf, where the flow was deflected by the topography of the eastern Ross sector. As the IVT cyclonically curved along the Transantarctic Mountains, leading to equatorward fluxes off the coasts of Victoria Land, the strongest temperature anomalies occurred and peaked over the Ross Ice Shelf. DARK ARs capture the complete curved moisture transport pathway responsible for this event, whereas the Wille schemes detect only the initial southward intrusion and miss the equatorward-turning segment beneath which the peak temperature anomalies occurred. G&W v4 detects the initial southward intrusion from the mid-latitudes and, like DARK, captures the moisture transport toward the Ross Ice Shelf where the peak temperature anomalies occurred, but its detection stops at the coastline. As on 1 December 2003, G&W v4 flags numerous AR objects across the hemisphere on this date, in contrast to the more sparse detections of DARK and the Wille schemes.

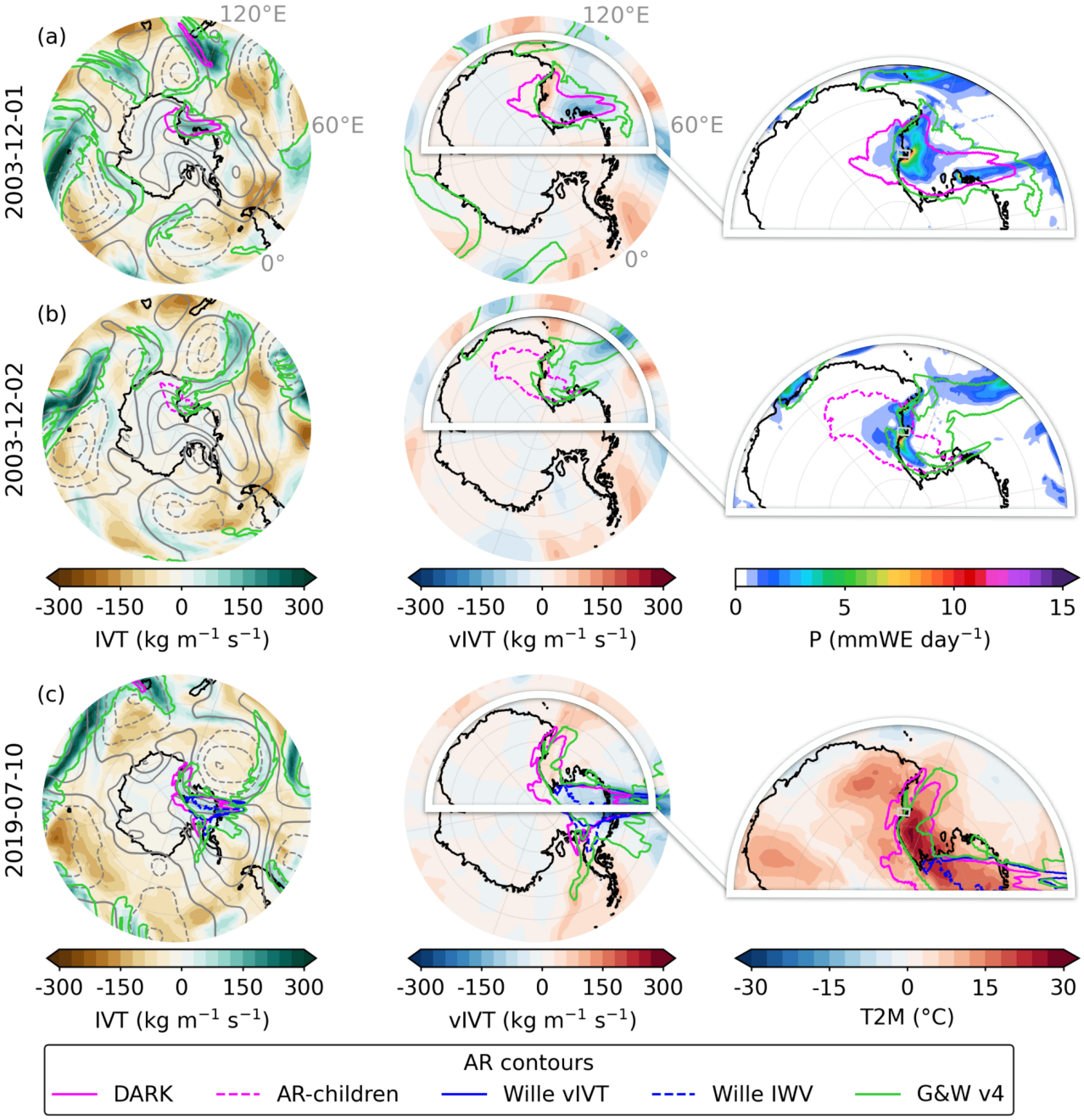

536

537 Figure 10. Daily composites of the most intense (a–b) precipitation and (c) temperature events in the McMurdo–Dry Valleys
538 region (160–168° E, 78.5–77.5° S, grey window in the third column panels). Panels (a) and (b) correspond to 1 and 2 December
539 2003, respectively, showing the evolution of the same precipitation event, while panel (c) shows the temperature event on 9
540 July 2019. Each column displays, from left to right: integrated vapor transport (IVT) anomaly (kg m^{-1} s^{-1}), meridional IVT

(vIVT) anomaly (kg m^{-1} s^{-1}), and (a–b) daily precipitation (mm w.e. day^{-1}) or (c) 2 m air temperature anomaly (°C). Grey contours in the first column indicate 500-hPa geopotential-height anomalies (m; solid = positive, dashed = negative) at 100-m intervals. DARK ARs (solid magenta) and their children (dashed magenta) are shown together with Wille ARs (solid blue = vIVT; dashed blue = IWV) and G&W v4 ARs (limegreen). For each day, AR contours represent the maximum spatial extent of each AR type across all 6-hourly time steps (i.e., the union of all detected positions within the day). White-shaded contours in the middle panels outline the domain shown in the rightmost panels.

3.4.2 ARs reaching the South Pole

One of the major advancements of the DARK framework is its ability to detect ARs reaching the South Pole, whereas previous schemes such as Wille vIVT and IWV ceased detection at 85° S. In ERA5, IVT vectors become ill-defined exactly at 90° S because of the coordinate singularity, which causes an artificial drop in detections at the pole. Nevertheless, DARK captures continuous poleward moisture transport all the way to the South Pole, enabling for the first time a physically consistent identification of ARs in this region. To illustrate this, we examine three events detected by DARK near the pole.

On 30 July 1991 (Fig. 11a), a DARK AR was detected extending from the Princess Elizabeth Land coast across the Antarctic interior to the South Pole. The synoptic configuration featured two centers of action, with a low-pressure system east of Princess Elizabeth Land and a high-pressure system farther east, jointly channeling the moisture plume poleward in a roller-like pattern. Both Wille vIVT and DARK identified ARs along this corridor on that day. However, the Wille vIVT AR stopped at the coast as the meridional IVT component weakened below the 98th percentile and the flow turned more zonal toward Dome A and the South Pole. Yet, the total IVT remained strong, allowing DARK to maintain continuous detection inland. G&W v4 detects multiple ARs around the continent on this date, including the AR of interest, but its detection stops shortly after the coastline. Under the AR footprint, 2 m air temperature anomalies already reached around +20 °C, reflecting the strong advection of warm, moist air from lower latitudes. On the following day, the IVT flow advanced farther across the East Antarctic Plateau. Both Wille and DARK detected ARs from the Princess Elizabeth Land coast over Dome A, with their extent broadening to cover areas from Dronning Maud Land to Victoria Land, reaching latitudes as far south as 85° S. G&W v4 follows the moisture plume slightly further inland than on the previous day. Temperature anomalies intensified in step with the AR progression, spreading across the southern flank of the EAID. By the third day, the Wille ARs were no longer detected, while the DARK AR spanned a broad region south of the EAID, reaching the South Pole with a tail still visible along the East Antarctic coast. G&W v4 had already regressed to the coastline, failing to track the moisture transport over the interior where the strongest temperature anomalies, approaching +27 °C, were now concentrated beneath and slightly downstream of the DARK AR core. The strongest temperature anomalies, approaching +27 °C, were recorded at this stage beneath and slightly downstream of the AR core. By the fourth day, the feature had contracted into a thinner filament along the southern flank of the EAID, while the residual warm anomalies persisted in the area previously impacted by the main AR.

On 11 May 2018 (Fig. 11b), intense moisture transport was directed toward Dronning Maud Land, similarly driven by a marked pressure dipole, with a high-pressure system to the east and a low to the west. Both Wille vIVT and DARK detect ARs in this configuration, but the DARK AR extends farther inland, reaching Queen Elizabeth Land and up to 87° S. G&W v4 follows the moisture transport more closely than the Wille schemes, detecting the AR along the Queen Elizabeth Land coastline and the Ronne–Filchner Ice Shelf. It also captures an additional AR approaching from the WAIS that is not detected by DARK or the Wille schemes, which may represent the precursor moisture flux that evolves into the DARK AR over the South Pole on the following day. This event coincides with widespread positive 2 m air temperature anomalies across most of the Antarctic Ice Sheet, except along the East Antarctic coast from Victoria Land to the Amery Ice Shelf. On the following day, no Wille AR was detected, while the DARK AR had evolved and split into two structures: an AR over the South Pole, just north of the Ross Ice Shelf where surface temperatures continued to rise, and an AR-child along the original AR path over Dronning Maud Land. G&W v4 no longer detects the interior feature, consistent with its inland detection limitations. By the third day, only the main DARK AR remained, now centered over and slightly beyond the South Pole, having crossed the EAID before being deflected westward by the topography. Beneath this AR, 2 m air temperature anomalies intensified further, locally reaching +20 °C. By the fourth day, the AR had decayed into a smaller AR-child, yet the warm anomalies remained strong, particularly within these moisture remnants. Notably, after the AR had moved away from Dronning Maud Land, temperature anomalies there continued to increase through days 3 and 4, suggesting that the warm air mass and its heat content persisted well after the main AR passage.

On 31 August 2020 (Fig. 11c), a moisture-laden plume reached the Ross Ice Shelf, similarly guided by a high-pressure system centered over West Antarctica and a low-pressure system over Victoria Land. The disorganized structure of both systems, with wavy rather than well-defined closed centers of action, reflects relatively weak wind speeds, which likely explains why this event is not detected by either vIVT or DARK. The event was detected as a Wille IWV AR and as a G&W v4 AR, extending from the South Pacific across Marie Byrd Land to the Ross Ice Shelf. At its southern tip, a portion of this AR was also classified as an AR-child, indicating sustained, concentrated moisture transport embedded within the broader IWV and IVT structure. This episode produced exceptionally strong surface temperature anomalies over the Ross Ice Shelf, locally exceeding +30 °C. On the following day, the anticyclonic anomaly shifted southward toward the South Pole, while the low-pressure system elongated eastward, forming a double-centered trough. Together, these systems established a broad zonal corridor that directed the DARK AR across the Antarctic interior. By the third day, the AR extended along the southern flank of the EAID, maintaining a coherent filament structure. G&W v4 still detects the feature on this day but its detection stops shortly after the coastline, failing to follow the moisture plume as it propagates inland with DARK. The warm anomalies migrated with the AR core, indicating active advection of heat and moisture along its path. By the fourth day, the AR weakened and contracted into a diminished AR structure centered near the South Pole and extending over southern Dronning Maud Land and southern Princess Elizabeth Land. Despite this decay, pronounced 2 m air temperature anomalies persisted over the region previously

covered by the main AR on day 3, rather than beneath the contracted AR-child itself, reflecting the lingering thermal influence of the moist and warm air mass advected during peak AR activity rather than active transport at this stage.

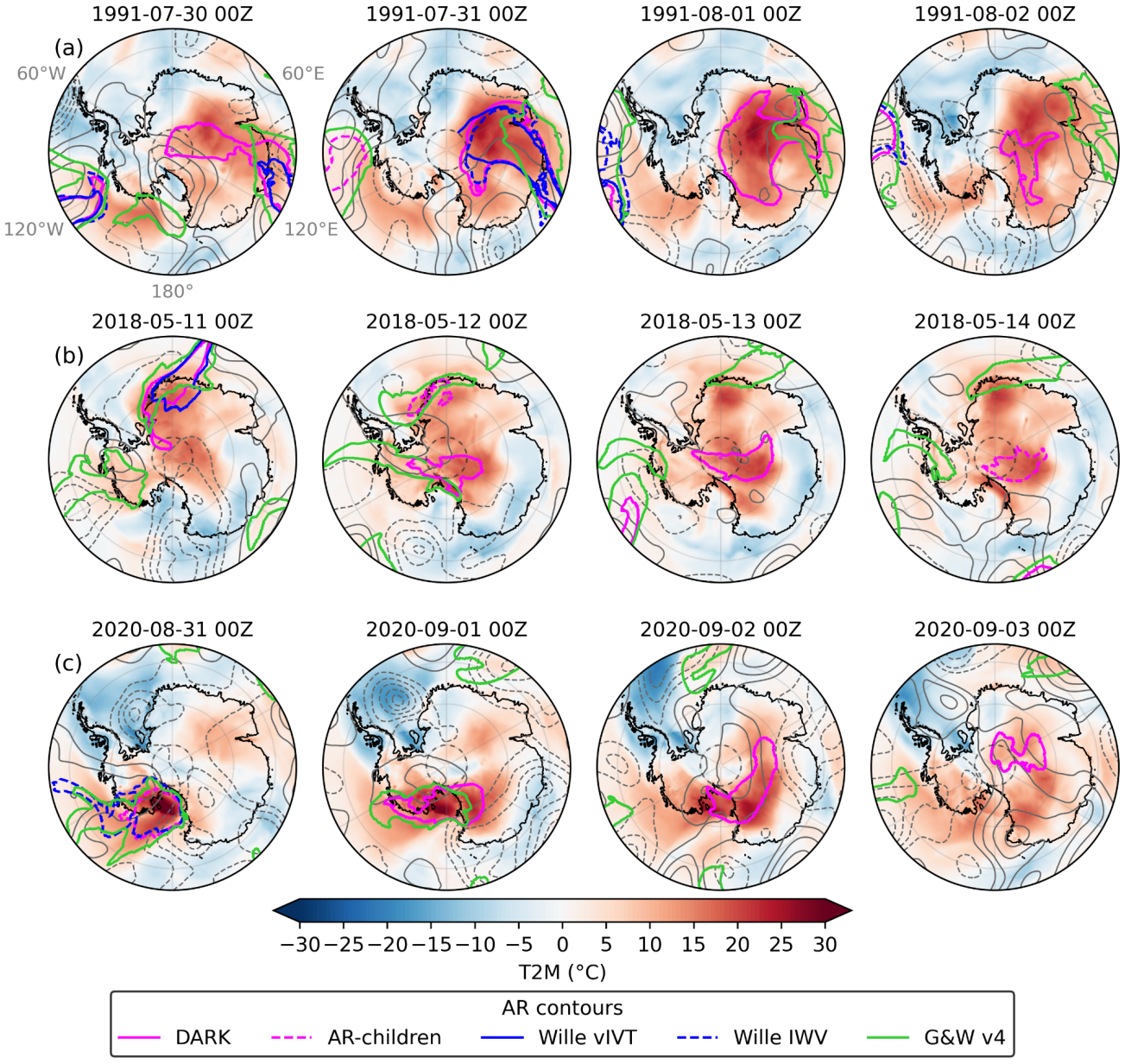

Figure 11. Synoptic evolution of three DARK AR events penetrating south of 85° S. Rows (a–c) correspond to the events from 30 July–2 August 1991, 11–14 May 2018, and 31 August–3 September 2020, respectively. Columns show sequential days at 00 UTC. Filled colors depict 2 m air temperature anomalies (° C), and grey contours show 500-hPa geopotential-height

anomalies (m; solid = positive, dashed = negative) at 50-m intervals. DARK ARs (solid magenta) and their children (dashed magenta) are shown together with Wille ARs (solid blue = vIVT; dashed blue = IWV) and G&W v4 ARs (limegreen). The dashed circle marks 85° S, and regions north of 60° S are masked.

4 Discussion & Conclusion

The DARK framework bridges the gap between the intensity-focused Antarctic schemes of Wille vIVT and IWV and the globally applied IVT-based approaches such as Guan and Waliser (2015, 2019), while extending the geometric flexibility recently introduced by Spensberger et al. (2025). Building on Wille's methods, DARK retains the strict 98th-percentile threshold to isolate the most intense moisture-transport events while introducing key advancements: it uses total IVT rather than only its meridional component and computes total filament length instead of meridional extent, thereby removing the directional and geometric constraints that previously limited the detection of curved or equatorward-turning ARs. Global IVT-based schemes such as Guan and Waliser (2015, 2019, 2024) also use IVT magnitude but impose a directional coherence constraint that may limit the detection of ARs with strongly curved or reversing geometries. By relaxing this requirement, DARK identifies dynamically coherent, non-meridional ARs that are common near the Antarctic coast, where synoptic steering, Coriolis deflection, and topographic deflection distort moisture pathways.

Unlike previous frameworks, DARK eliminates the artificial boundary effects that limited AR detection close to the poles. In Wille vIVT, the reversal of the meridional IVT component at the South Pole prevents continuous detection of pole-crossing features, while the 20° meridional extent criterion introduces a secondary edge effect up to about 65° S. The Wille IWV scheme avoids the vIVT singularity but remains affected by this geometric limitation, because it was developed and applied assuming a southward boundary at 85°S. G&W v4 avoids these specific boundary issues but introduces a different spatial limitation: its hemispheric IVT threshold is very permissive along the coast and over West Antarctica, generating far more AR detections than DARK or the Wille schemes in these regions, while being very restrictive over the cold, dry East Antarctic interior, where its effective threshold prevents detection of the weaker but climatologically relevant moisture intrusions that DARK and Wille capture. This results in a highly heterogeneous detection footprint, with overdetection at the coast and underdetection inland, and only a narrow transitional zone where detection frequencies are broadly comparable to those of DARK or the Wille schemes. This reflects the fundamental mismatch between a hemispheric IVT threshold and the strong spatial gradients in Antarctic IVT climatology, making G&W v4 better suited for characterizing coastal AR activity rather than tracking AR influence across the full Antarctic continent and into the interior. By using total IVT and defining the 2,000 km minimum extent along the full curved axis of the filament rather than its meridional projection, DARK, together with the AR-children add-on, enables continuous tracking of ARs throughout their lifecycle, from oceanic genesis across the Antarctic continent and occasionally the South Pole to their inland decay and fragmentation as AR-children. This provides a seamless representation of poleward moisture transport and its persistence over the ice sheet.

The climatology derived from DARK ARs is broadly consistent with that of Wille vIVT and IWV, confirming that it preserves the physical realism of established Antarctic AR frameworks. A majority of Wille ARs are detected by DARK, and overall AR frequency along the Antarctic coast remains similar to that obtained with Wille's schemes, indicating strong agreement to detect the initial moisture intrusions. This shows that the method extends rather than replaces previous approaches: Wille ARs represent some of the most intense events, accounting for much of the precipitation and extreme anomalies. DARK additionally identifies ARs systematically missed by Wille's directional and geometric constraints. These new detections occur mainly south of the EAID, but additional events are found across the continent wherever moisture plumes turn zonally or overturn under the combined influence of vorticity and topography. These ARs are dynamically coherent systems associated with strong precipitation, pronounced temperature anomalies, and compound extremes. Their frequency aligns with the 20 % of extratropical moisture-transport axes that turn equatorward beyond 70° S (Spensberger et al., 2025), although the proportion is smaller here (about 6 %), suggesting that the most intense filaments, such as those detected by Wille, are less likely to overturn than weaker or more diffuse transports. While Wille vIVT remains most effective at isolating direct, intense poleward intrusions, DARK complements it by capturing a broader spectrum of AR geometries that are still physically meaningful and climatically relevant.

DARK ARs account for an average of 18 % of total Antarctic precipitation, compared to about 13 % in Wille vIVT. The largest increases occur in coastal embayments and across catchments south of the EAID, where the inclusion of AR-children further amplifies local contributions, raising them from only a few percent in Wille vIVT to over 20 %. This rise does not result from more intense precipitation within individual events but from a higher occurrence and greater diversity of ARs detected by DARK. On average, individual DARK ARs are associated with slightly lower mean precipitation per event than Wille ARs, which remain the most precipitation-intense. However, DARK also identifies additional ARs that are moderately weaker while still belonging to the upper tail of the precipitation distribution. In particular, DARK captures a larger fraction of precipitation extremes, as defined above by the daily 99th-percentile anomaly, with the strongest signals in regions such as McMurdo, Victoria Land, and near the South Pole south of the EAID. A similar pattern emerges for 2 m air temperature and compound extremes, where DARK detects more events than Wille. Risk ratio analysis confirms that this stronger association with extremes is not simply a by-product of higher AR frequency: extreme events are statistically more likely to occur during DARK ARs than during Wille ARs, and even more so when AR-children are included. The comparison with G&W v4 reveals a contrasting picture for both precipitation attribution and risk ratios. While G&W v4 explains more total precipitation along the coast and over West Antarctica due to its high detection frequency in these regions, DARK explains substantially more inland, particularly north of the EAID where G&W v4 detections drop sharply. For extreme events, the same coastal-to-inland polarity applies, but the continent-wide mean difference remains positive in favor of DARK, as the abundance of G&W v4 coastal detections inevitably captures most extreme days by volume while attributing a large share of precipitation to non-extreme events. The very high RR values of G&W v4 along the coast reflect this detection structure. Conversely, inland where G&W v4 detections are sparse, the few detected ARs are almost exclusively associated with extreme events, while the vast non-AR

pool again drives the denominator toward zero. In both cases, the RR is not physically comparable to that of DARK or the Wille schemes, which maintain a spatially consistent detection range across the continent. This highlights a general limitation of the RR metric when comparing ARDTs with strongly contrasting detection frequencies: RR conflates physical association strength with detection selectivity, and should be interpreted alongside occurrence and fraction of extremes explained when assessing cross-ARDT performance.

Another key contribution of this work lies in the introduction of the AR-children module, which extends detection beyond landfall by identifying remnants with high moisture transport that remain dynamically connected to their parent ARs. As ARs encounter the Antarctic coast, condensation, latent heating, and orographic deflection often disrupt their filamentary structure, causing them to fall below the length or coherence thresholds of conventional algorithms. These fragments, although shorter, maintain IVT above the 98th percentile and continue to produce significant precipitation and temperature anomalies inland. The AR-children algorithm captures these post-landfall features, enabling the representation of the decaying yet dynamically active stages of the ARs (Wille et al., 2024). In Antarctica, AR-children are particularly important over Victoria Land and the Amery Ice Shelf, where they account for more than 8 % of total precipitation and contribute up to 20 % of all extreme events, including precipitation, temperature, and compound extremes. When AR-children are included in addition to DARK ARs, the mean association with precipitation extremes increases from 53 % to 58 %, with temperature extremes from 67 % to 71 %, and with compound extremes from 80 % to 83 %. These results demonstrate that AR-children are not marginal phenomena but intrinsic components of the Antarctic AR lifecycle, representing the decaying inland phase of ARs and accounting for their delayed effects on precipitation and temperature extremes. From a practical standpoint, users whose focus is limited to coastal AR landfalls and their immediate impacts may find the core DARK algorithm sufficient, given its substantially lower computational cost, while the AR-children module is recommended for studies focusing on inland moisture transport and surface impacts.

Despite these advances, DARK remains subject to methodological assumptions that introduce uncertainty. A minimum AR length of 2,000 km was imposed to match the typical scale of ARs described in the literature (e.g., Guan and Waliser, 2015; Wille et al., 2021; Skinner et al., 2020; Gorodetskaya et al., 2014), generally longer than 2,000 km and narrower than 1,000 km. DARK does not explicitly constrain AR width, as the use of IVT naturally favors elongated structures, in contrast with IWV-based schemes that can produce broad, static moisture plumes. The AR-children module further applies a minimum feature area of 20,000 km² to remove small, short-lived moisture patches. This threshold is not physically based but chosen pragmatically to exclude spurious, localizedpost-landfall features. These thresholds are empirically motivated by case-study analyses, which show that post-AR moist structures typically extend over at least this spatial scale. While a comprehensive sensitivity analysis is beyond the scope of this study, future work could further explore how varying these thresholds affects detection frequency and precipitation attribution. Likewise, the 15-day rolling window used to compute the 98th-percentile IVT threshold improves upon monthly percentiles by avoiding discontinuities at month boundaries, but it adds complexity that

may affect reproducibility. These design choices illustrate the necessary balance between physical robustness and algorithmic simplicity inherent to percentile-based detection frameworks.

As with all threshold-based methods, DARK defines discrete events within a continuous moisture field. The 98th-percentile threshold represents both an empirical compromise between inclusiveness and selectivity and a deliberate choice to ensure methodological continuity with previous Antarctic AR frameworks, particularly Wille vIVT and IWV. Lowering the threshold would inflate detections but weaken dynamical coherence, while raising it would isolate too few, overly intense events. Retaining the 98th percentile thus preserves comparability with earlier studies while providing a pragmatic balance that isolates physically meaningful ARs and maintains statistical consistency. Future work could explore adaptive thresholds that evolve with temperature, such as those proposed by Barthélemy et al. (2025) and Maclennan et al. (2025), to better represent thermodynamic scaling under warming conditions and to extend the applicability of DARK and related tools across diverse climate states, from palaeoclimate to future projections.

Overall, DARK provides a coherent and physically consistent framework for characterizing Antarctic ARs and their climatic influence. By removing directional and geometric constraints, eliminating artificial boundaries at the pole, and, with the add-on incorporating post-landfall detection through AR-children, it allows continuous tracking of ARs from oceanic genesis to polar dissipation. In doing so, DARK better captures the full lifecycle of Antarctic ARs, from their formation in the lower latitudes, through landfall and inland decay, including a potential passage across the South Pole, thereby providing an unprecedentedly complete view of AR-driven moisture and energy transport over the Antarctic Ice Sheet. In addition to further highlighting the SMB impacts of ARs across the entire Antarctic Ice Sheet as seen here, DARK provides a tool for tracking the influence of residual AR moisture on Antarctic mesoscale-scale atmospheric dynamics like polar lows and barrier jets (Carrasco and Bromwich, 1993; Nigro et al., 2012). This framework bridges global and polar perspectives, linking large-scale moisture transport pathways to regional precipitation, temperature, and compound extremes over the Antarctic Ice Sheet, and highlighting that the influence of ARs extends well beyond their initial landfall.

Code and data availability

The DARK algorithm was developed in Python and is publicly available under an open-source license at https://github.com/victoirebuffet/DARK_atmospheric_river_detection_tool. The detection and analysis scripts rely on standard Python libraries including xarray, numpy, scipy, matplotlib, and cartopy, and are designed to process ERA5 reanalysis data in NetCDF format, however codes were made for MERRA-2 and CESM-LE2, codes are available upon request. ERA5 reanalysis data (Hersbach et al., 2023a; Hersbach et al., 2023b) are available from the Copernicus Climate Data Store (CDS) at https://cds.climate.copernicus.eu/. The DARK AR catalog is available at https://doi.org/10.5281/zenodo.17963007, while the DARK AR+children catalog is available at https://doi.org/10.5281/zenodo.17962931. The AR-children detection module requires substantially more computational resources than the core DARK algorithm. Processing the full 1979–2023 ERA5

climatology in a single run requires approximately 9h of CPU time and ~17 GB of memory on a single CPU core, compared to 1h and ~8 GB for the core DARK algorithm. Users requiring only AR detection without post-landfall remnant tracking can therefore run DARK at negligible computational cost, while the AR-children module is recommended for studies focusing on inland moisture transport or the full AR life cycle. AR catalogs for Wille vIVT and Wille IWV, re-run from the method of Wille et al. (2021), on the full period of study (1979–2023), are available at https://doi.org/10.5281/zenodo.17968902.

Author contributions

VB developed the detection algorithms, curated and analyzed the data, and prepared the initial draft of the manuscript, including figures and visualizations. VF and BP guided the investigation, and contributed to refining the final version of the manuscript. JW contributed to the conceptual development of the study, provided scientific guidance throughout the research process, and contributed to revising the final manuscript.

Competing interests

The authors declare that they have no conflict of interest.

Financial support

This research has been supported by the Agence Nationale de la Recherche (ANR) under project ANR-20-CE01-0013 (ARCA).

Acknowledgements

We thank the European Centre for Medium-Range Weather Forecasts (ECMWF) for providing the ERA5 reanalysis data. We thank Juliette Blanchet for valuable feedback on the significance testing. We thank Bin Guan for kindly providing the G&W v4 AR catalogue. We thank the two anonymous reviewers whose constructive comments improved the manuscript. We thank the developers of python, matplotlib, cartopy, xarray, scipy, numpy, scikit-image, geopy, netcdf4, networkx and pandas. Calculations were performed using HPC resources from DNUM CCUB (Centre de Calcul de l'Université Bourgogne Europe).

References

Adusumilli, S., A. Fish, M., Fricker, H. A., and Medley, B.: Atmospheric River Precipitation Contributed to Rapid Increases in Surface Height of the West Antarctic Ice Sheet in 2019, Geophysical Research Letters, 48, e2020GL091076, https://doi.org/10.1029/2020GL091076, 2021.

American Meteorological Society, Glossary of Meteorology: Atmospheric River. https://glossary.ametsoc.org/wiki/Atmospheric-river, 2022.

Barthélemy, L., Codron, F., Wille, J.,Favier, V., & Clem, K. R.: Future atmospheric rivers in Antarctica: Characteristics and impacts with the IPSL model. Journal of Geophysical Research: Atmospheres, 130, e2025JD043398. https://doi.org/10.1029/2025JD043398, 2025.

Carrasco, J. F. and Bromwich, D. H.: Mesoscale cyclogenesis dynamics over the southwestern Ross Sea, Antarctica, Journal of Geophysical Research: Atmospheres, 98, 12973–12995, https://doi.org/10.1029/92JD02821, 1993.

Chang, E. K. M., Lee, S., and Swanson, K. L.: Storm Track Dynamics, Journal of Climate, 15, 2163–2183, https://doi.org/10.1175/1520-0442(2002)015%253C02163:STD%253E2.0.CO;2, 2002.

Chemke, R., Zanna, L., Orbe, C., Sentman, L. T., and Polvani, L. M.: The Future Intensification of the North Atlantic Winter Storm Track: The Key Role of Dynamic Ocean Coupling, Journal of Climate, 35, 2407–2421, https://doi.org/10.1175/JCLI-D-21-0407.1, 2022.

Collow, A. B. M., Shields, C. A., Guan, B., Kim, S., Lora, J. M., McClenny, E. E., Nardi, K., Payne, A., Reid, K., Shearer, E. J., Tomé, R., Wille, J. D., Ramos, A. M., Gorodetskaya, I. V., Leung, L. R., O'Brien, T. A., Ralph, F. M., Rutz, J., Ullrich, P. A., and Wehner, M.: An Overview of ARTMIP's Tier 2 Reanalysis Intercomparison: Uncertainty in the Detection of Atmospheric Rivers and Their Associated Precipitation, Journal of Geophysical Research: Atmospheres, 127, e2021JD036155, https://doi.org/10.1029/2021JD036155, 2022.

Dacre, H. F. and Clark, P. A.: A kinematic analysis of extratropical cyclones, warm conveyor belts and atmospheric rivers, npj Clim Atmos Sci, 8, 97, https://doi.org/10.1038/s41612-025-00942-z, 2025.

Gorodetskaya, I. V., Tsukernik, M., Claes, K., Ralph, M. F., Neff, W. D., and Van Lipzig, N. P. M.: The role of atmospheric rivers in anomalous snow accumulation in East Antarctica, Geophysical Research Letters, 41, 6199–6206, https://doi.org/10.1002/2014GL060881, 2014.

Gorodetskaya, I. V., Durán-Alarcón, C., González-Herrero, S., Clem, K. R., Zou, X., Rowe, P., Rodriguez Imazio, P., Campos, D., Leroy-Dos Santos, C., Dutrievoz, N., Wille, J. D., Chyhareva, A., Favier, V., Blanchet, J., Pohl, B., Cordero, R. R., Park, S.-J., Colwell, S., Lazzara, M. A., Carrasco, J., Gulisano, A. M., Krakovska, S., Ralph, F. M., Dethinne, T., and Picard, G.: Record-high Antarctic Peninsula temperatures and surface melt in February 2022: a compound event with an intense atmospheric river, npj Clim Atmos Sci, 6, 1–18, https://doi.org/10.1038/s41612-023-00529-6, 2023.

Guan, B. and Waliser, D. E.: Detection of atmospheric rivers: Evaluation and application of an algorithm for global studies: Detection of Atmospheric Rivers, J. Geophys. Res. Atmos., 120, 12514–12535, https://doi.org/10.1002/2015JD024257, 2015.

Guan, B. and Waliser, D. E.: Tracking Atmospheric Rivers Globally: Spatial Distributions and Temporal Evolution of Life Cycle Characteristics, Journal of Geophysical Research: Atmospheres, 124, 12523–12552, https://doi.org/10.1029/2019JD031205, 2019.

Guan, B. and Waliser, D. E.: A regionally refined quarter-degree global atmospheric rivers database based on ERA5, Scientific Data, 11, 440, https://doi.org/10.1038/s41597-024-03258-4, 2024.

Hersbach, H., Bell, B., Berrisford, P., Hirahara, S., Horányi, A., Muñoz-Sabater, J., Nicolas, J., Peubey, C., Radu, R., Schepers, D., Simmons, A., Soci, C., Abdalla, S., Abellan, X., Balsamo, G., Bechtold, P., Biavati, G., Bidlot, J., Bonavita, M., De Chiara, G., Dahlgren, P., Dee, D., Diamantakis, M., Dragani, R., Flemming, J., Forbes, R., Fuentes, M., Geer, A., Haimberger, L., Healy, S., Hogan, R. J., Hólm, E., Janisková, M., Keeley, S., Laloyaux, P., Lopez, P., Lupu, C., Radnoti, G., De Rosnay, P., Rozum, I., Vamborg, F., Villaume, S., and Thépaut, J.: The ERA5 global reanalysis, Quart J Royal Meteoro Soc, 146, 1999–2049, https://doi.org/10.1002/qj.3803, 2020.

Hersbach, H., Bell, B., Berrisford, P., Biavati, G., Horányi, A., Muñoz Sabater, J., Nicolas, J., Peubey, C., Radu, R., Rozum, I., Schepers, D., Simmons, A., Soci, C., Dee, D., Thépaut, J-N.: ERA5 hourly data on pressure levels from 1940 to present. Copernicus Climate Change Service (C3S) Climate Data Store (CDS), DOI: https://doi.org/10.24381/cds.bd0915c6, 2023a.

Hersbach, H., Bell, B., Berrisford, P., Biavati, G., Horányi, A., Muñoz Sabater, J., Nicolas, J., Peubey, C., Radu, R., Rozum, I., Schepers, D., Simmons, A., Soci, C., Dee, D., Thépaut, J-N. : ERA5 hourly data on single levels from 1940 to present. Copernicus Climate Change Service (C3S) Climate Data Store (CDS) : https://doi.org/10.24381/cds.adbb2d47, 2023b.

Katz, D., Baptista, J., Azen, S. P., and Pike, M. C.: Obtaining Confidence Intervals for the Risk Ratio in Cohort Studies, Biometrics, 34, 469–474, https://doi.org/10.2307/2530610, 1978.

Maclennan, M. L., Lenaerts, J. T. M., Shields, C., and Wille, J. D.: Contribution of Atmospheric Rivers to Antarctic Precipitation, Geophysical Research Letters, 49, e2022GL100585, https://doi.org/10.1029/2022GL100585, 2022.

Maclennan, M. L., Winters, A. C., Shields, C. A., Thaker, R., Barthelemy, L., Codron, F., and Wille, J. D.: Rising atmospheric moisture escalates the future impact of atmospheric rivers in the Antarctic climate system, Commun Earth Environ, 6, 369, https://doi.org/10.1038/s43247-025-02333-x, 2025.

Mattingly, K. S., Mote, T. L., and Fettweis, X.: Atmospheric River Impacts on Greenland Ice Sheet Surface Mass Balance, Journal of Geophysical Research: Atmospheres, 123, 8538–8560, https://doi.org/10.1029/2018JD028714, 2018.

Nigro, M. A., Cassano, J. J., Lazzara, M. A., and Keller, L. M.: Case Study of a Barrier Wind Corner Jet off the Coast of the Prince Olav Mountains, Antarctica, Monthly Weather Review, 140, 2044–2063, https://doi.org/10.1175/MWR-D-11-00261.1, 2012.

Scholz, S. R. and Lora, J. M.: Atmospheric rivers cause warm winters and extreme heat events, Nature, 636, 640–646, https://doi.org/10.1038/s41586-024-08238-7, 2024.

Skinner, C. B., Lora, J. M., Payne, A. E., and Poulsen, C. J.: Atmospheric river changes shaped mid-latitude hydroclimate since the mid-Holocene, Earth and Planetary Science Letters, 541, 116293, https://doi.org/10.1016/j.epsl.2020.116293, 2020.

Spensberger, C., Konstali, K., and Spengler, T.: Moisture transport axes: a unifying definition for tropical moisture exports, atmospheric rivers, and warm moist intrusions, Weather and Climate Dynamics, 6, 431–446, https://doi.org/10.5194/wcd-6-431-2025, 2025.

Turner, J., Phillips, T., Thamban, M., Rahaman, W., Marshall, G. J., Wille, J. D., Favier, V., Winton, V. H. L., Thomas, E., Wang, Z., van den Broeke, M., Hosking, J. S., and Lachlan-Cope, T.: The Dominant Role of Extreme Precipitation Events in Antarctic Snowfall Variability, Geophysical Research Letters, 46, 3502–3511, https://doi.org/10.1029/2018GL081517, 2019.

Wille, J. D., Favier, V., Dufour, A., Gorodetskaya, I. V., Turner, J., Agosta, C., and Codron, F.: West Antarctic surface melt triggered by atmospheric rivers, Nat. Geosci., 12, 911–916, https://doi.org/10.1038/s41561-019-0460-1, 2019.

Wille, J. D., Favier, V., Gorodetskaya, I. V., Agosta, C., Kittel, C., Beeman, J. C., Jourdain, N. C., Lenaerts, J. T. M., and Codron, F.: Antarctic Atmospheric River Climatology and Precipitation Impacts, Journal of Geophysical Research: Atmospheres, 126, https://doi.org/10.1029/2020jd033788, 2021.

Wille, J. D., Favier, V., Jourdain, N. C., Kittel, C., Turton, J. V., Agosta, C., Gorodetskaya, I. V., Picard, G., Codron, F., Santos, C. L.-D., Amory, C., Fettweis, X., Blanchet, J., Jomelli, V., and Berchet, A.: Intense atmospheric rivers can weaken ice shelf stability at the Antarctic Peninsula, Commun Earth Environ, 3, 1–14, https://doi.org/10.1038/s43247-022-00422-9, 2022.

Wille, J. D., Pohl, B., Favier, V., Winters, A. C., Baiman, R., Cavallo, S. M., Leroy-Dos Santos, C., Clem, K., Udy, D. G., Vance, T. R., Gorodetskaya, I., Codron, F., and Berchet, A.: Examining Atmospheric River Life Cycles in East Antarctica, Journal of Geophysical Research: Atmospheres, 129, e2023JD039970, https://doi.org/10.1029/2023JD039970, 2024.

Wille, J. D., Favier, V., Gorodetskaya, I. V., Agosta, C., Baiman, R., Barrett, J. E., Barthelemy, L., Boza, B., Bozkurt, D., Casado, M., Chyhareva, A., Clem, K. R., Codron, F., Datta, R. T., Durán-Alarcón, C., Francis, D., Hoffman, A. O., Kolbe, M., Krakovska, S., Linscott, G., Maclennan, M. L., Mattingly, K. S., Mu, Y., Pohl, B., Santos, C. L.-D., Shields, C. A., Toker, E., Winters, A. C., Yin, Z., Zou, X., Zhang, C., and Zhang, Z.: Atmospheric rivers in Antarctica, Nat Rev Earth Environ, 6, 178–192, https://doi.org/10.1038/s43017-024-00638-7, 2025.

Wirth, V., Riemer, M., Chang, E. K. M., and Martius, O.: Rossby Wave Packets on the Midlatitude Waveguide—A Review, Monthly Weather Review, 146, 1965–2001, https://doi.org/10.1175/MWR-D-16-0483.1, 2018.

Zhu, Y. and Newell, R. E.: A Proposed Algorithm for Moisture Fluxes from Atmospheric Rivers, Monthly Weather Review, 126, 725–735, https://doi.org/10.1175/1520-0493(1998)126<0725:APAFMF>2.0.CO;2, 1998.